

AD-A179 931

DETERMINATION OF THE LOCAL HEAT TRANSFER
CHARACTERISTICS ON GLAZE ICE ACC (U) KENTUCKY UNIV
LEXINGTON DEPT OF MECHANICAL ENGINEERING

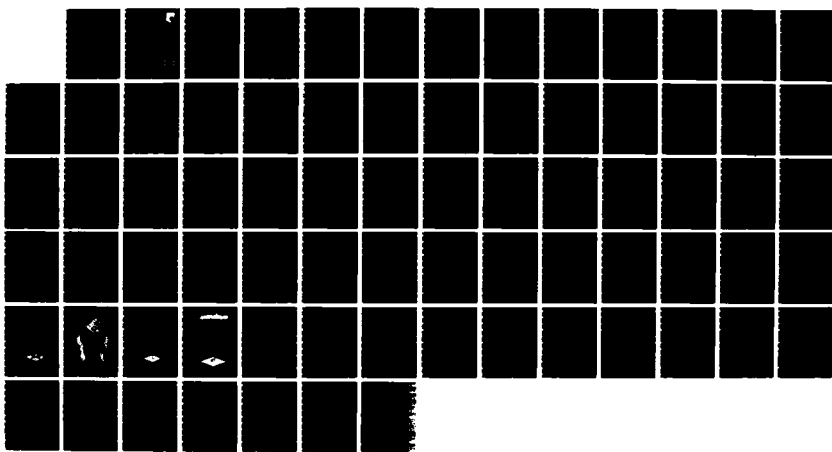
UNCLASSIFIED

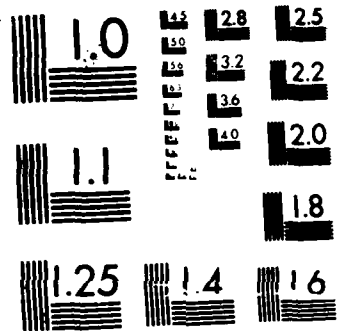
M R PAIS ET AL APR 87 AFWAL-TR-87-3001

1/1

F/G 28/4

NL





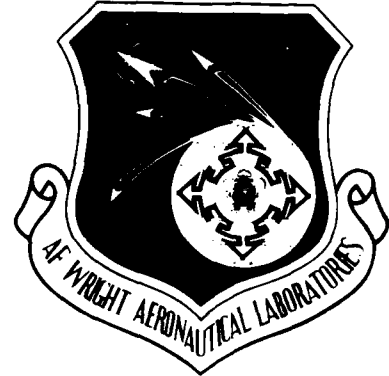
MICROCOPY RESOLUTION TEST CHART
NATIONAL BUREAU OF STANDARDS 1964 A

AD-A179 931

DTIC FILE COPY

AFWAL-TR-87-3001

DETERMINATION OF THE LOCAL HEAT TRANSFER CHARACTERISTICS ON
GLAZE ICE ACCRETIONS ON A CYLINDER AND A NACA 0012 AIRFOIL



M.R. Pais
S.N. Singh

University of Kentucky
Department of Mechanical Engineering
Lexington KY 40506

April 1987

Final Report for Period May 1983 - September 1986

Approved for public release; distribution is unlimited

DTIC
ELECTED
MAY 05 1987
S E D
~~S E~~

FLIGHT DYNAMICS LABORATORY
AIR FORCE WRIGHT AERONAUTICAL LABORATORIES
AIR FORCE SYSTEMS COMMAND
WRIGHT-PATTERSON AIR FORCE BASE, OHIO 45433-6553

87 5 1 003

NOTICE

When Government drawings, specifications, or other data are used for any purpose other than in connection with a definitely related Government procurement operation, the United States Government thereby incurs no responsibility nor any obligation whatsoever; and the fact that the government may have formulated, furnished, or in any way supplied the said drawings, specifications, or other data, is not to be regarded by implication or otherwise as in any manner licensing the holder or any other person or corporation, or conveying any rights or permission to manufacture use, or sell any patented invention that may in any way be related thereto.

This report has been reviewed by the Office of Public Affairs (ASD/PA) and is releasable to the National Technical Information Service (NTIS). At NTIS, it will be available to the general public, including foreign nations.

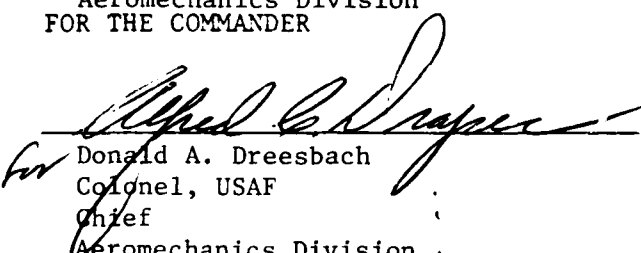
This technical report has been reviewed and is approved for publication.



Wladimiro Calarese
Aerospace Engineer
High Speed Aero Performance Branch
Aeromechanics Division
FOR THE COMMANDER



Valentine Dahlem
Chief
High Speed Aero Performance Branch
Aeromechanics Division


for
Donald A. Dreesbach
Colonel, USAF
Chief
Aeromechanics Division

"If your address has changed, if you wish to be removed from our mailing list, or if the addressee is no longer employed by your organization please notify AFWAL/FIMG, W-PAFB, OH 45433-6553 to help us maintain a current mailing list".

Copies of this report should not be returned unless is required by security considerations, contractual obligations, or notice on a specific document.

UNCLASSIFIED

SECURITY CLASSIFICATION OF THIS PAGE

110-1179-721

Form Approved
OMB No. 0704-0188

REPORT DOCUMENTATION PAGE			
1a. REPORT SECURITY CLASSIFICATION UNCLASSIFIED		1b. RESTRICTIVE MARKINGS	
2a. SECURITY CLASSIFICATION AUTHORITY		3 . DISTRIBUTION/AVAILABILITY OF REPORT Approved for Public release; distribution is unlimited.	
2b. DECLASSIFICATION/DOWNGRADING SCHEDULE			
4. PERFORMING ORGANIZATION REPORT NUMBER(S)		5. MONITORING ORGANIZATION REPORT NUMBER(S) AFWAL-TR-87-3001	
6a. NAME OF PERFORMING ORGANIZATION University of Kentucky	6b. OFFICE SYMBOL (if applicable)	7a. NAME OF MONITORING ORGANIZATION Air Force Wright Aeronautical Laboratories Flight Dynamics Laboratory (AFWAL/FIMG)	
6c. ADDRESS (City, State, and ZIP Code) Lexington Kentucky 40506		7b. ADDRESS (City, State, and ZIP Code) Wright-Patterson Air Force Base, OH 45433-6553	
8a. NAME OF FUNDING / SPONSORING ORGANIZATION		9. PROCUREMENT INSTRUMENT IDENTIFICATION NUMBER F33615-83-3013	
8c. ADDRESS (City, State, and ZIP Code)		10. SOURCE OF FUNDING NUMBERS	
		PROGRAM ELEMENT NO. 61102F	PROJECT NO. 2307
		TASK NO. N6	WORK UNIT ACCESSION NO. 08
11. TITLE (Include Security Classification) Determination of the local heat transfer characteristics on Glaze Ice Accretion on a cylinder and a NACA0012 Airfoil.			
12. PERSONAL AUTHOR(S) M.R. Pais and S.N. Singh			
13a. TYPE OF REPORT Final Report	13b. TIME COVERED FROM May 83 TO Sep 86	14. DATE OF REPORT (Year, Month, Day) April 1987	15. PAGE COUNT 72
16. SUPPLEMENTARY NOTATION			
17. COSATI CODES		18. SUBJECT TERMS (Continue on reverse if necessary and identify by block number)	
FIELD 0101	GROUP 2004	SUB-GROUP 0103	
19. ABSTRACT (Continue on reverse if necessary and identify by block number) Laboratory scale experiments were conducted in the subsonic wind tunnel facility at the University of Kentucky. Experimental convective local heat transfer coefficients were obtained for a simulated, full scale, selected set of 2, 5, and 15 minute glaze ice models on a cylinder and 0, 5 minute glaze ice models on a NACA 0012 airfoil. A steady state heat flux method was employed. The Nusselt numbers obtained in the Reynolds number range for cylinders of 100,000 to 150,000 are compared with published results. The results show very good quantitative and qualitative agreement. The local heat transfer rate increases with increasing Reynolds number and appears to decrease as the ice grows. Local Nusselt numbers for a smooth NACA 0012 airfoil at angles of attack $\alpha=0$, 2, 4, 6 and 8° and on a 5 minute smooth glaze ice shape on the same airfoil at $\alpha=4^\circ$ were also obtained. A number of experiments were performed in the Reynolds number range of 700,000 to 2,000,000, based on chord. A two-dimensional Fourier analysis is applied to surface profiles of a 15 minute glaze ice accretion on a cylinder to calculate the amplitude and wave length (Cont'd)			
20. DISTRIBUTION/AVAILABILITY OF ABSTRACT <input checked="" type="checkbox"/> UNCLASSIFIED/UNLIMITED <input type="checkbox"/> SAME AS RPT. <input type="checkbox"/> DTIC USERS		21. ABSTRACT SECURITY CLASSIFICATION UNCLASSIFIED	
22a. NAME OF RESPONSIBLE INDIVIDUAL Wladimiro Calarese		22b. TELEPHONE (Include Area Code) (513) 255-2052	22c. OFFICE SYMBOL AFWAL/FIMG

Block 19 (Cont'd)

of the surface roughness. The roughness k , is given in terms of amplitude, the width and spacing between the elements being specified by the inverse of the frequency. No single Sand Grain Roughness k can be assigned. Measurements of local Nusselt numbers and velocity fields are presented. When compared to results of smooth glaze ice models, the local Nusselt number for the rough models, shows an increase primarily at the top of the horn of up to 115%. Within the forward stagnation region, the increase may be partially attributed to the increase in area subtended by the roughness elements to the flow. It is deduced that the high amplitude low frequency components of the surface profile determine the fluid and thermal characteristics of the flow field.

TABLE OF CONTENTS

	PAGE
CHAPTER 1	1
INTRODUCTION	1
ICE FORMATION	2
EXPERIMENTAL PROGRAM	4
CHAPTER 2	6
EXPERIMENTAL METHODS	6
APPARATUS	8
EXPERIMENTAL PROCEDURE	10
2 MINUTE GLAZE ICE ON A CIRCULAR CYLINDER	12
5 MINUTE GLAZE ICE ON A CIRCULAR CYLINDER	13
15 MINUTE GLAZE ICE ON A CIRCULAR CYLINDER	14
CHAPTER 3	16
ROUGHNESS DEFINITION	16
THEORY	17
FABRICATION	22
FOURIER ANALYSIS	24
ROUGHNESS DESCRIPTION	27
SAND GRAIN ROUGHNESS	28
HEAT TRANSFER CHARACTERISTICS	33
CHAPTER 4	37
FABRICATION	37
RESULTS	38
CONCLUSIONS	40
ACKNOWLEDGEMENTS	42
FIGURES	43
TABLES	56
REFERENCES	62

LIST OF FIGURES

	PAGE
FIG. (1) 2, 5, 15 Glaze Ice Profiles	43
FIG. (2) Heater and Thermocouple Layout on Ice Model	43
FIG. (3) Local Nusselt Number on Cylinder and Airfoil	44
FIG. (4) Local Nusselt Number on 2 Minute Model	44
FIG. (5) Local Nusselt Number on 5 Minute Model	45
FIG. (6) Local Nusselt Number on 15 Minute Model	45
FIG. (7) Velocity Field Upstream of 15 Minute Smooth Model	46
FIG. (8) Comparison of Local Nusselt Number with Ice Growth	46
FIG. (9a) Surface Profile $h(x,y)$	47
FIG. (9b) 2-D FFT $H(m,n)$	47
FIG. (10) True Surface Profiles of 15 Minute Model	48
FIG. (11) Heater and Thermocouple Layout on Rough Ice Model	49
FIG. (12) 2-D FFT $R(F_x, F_z)$	49
FIG. (13a) 15 Minute Rough Skin Surface Profile	50
FIG. (13b) 15 Minute Rough Skin Profiles	50
FIG. (13c) 2-D FFT $H(F_x, F_y)$	50
FIG. (14) Velocity Field Around 15 Minute Rough Model	51
FIG. (15) Local Nusselt Number Using Plan Area	51
FIG. (16) Local Nusselt Number Using True Area	52
FIG. (17) Local Nusselt Number(C) on 0 Minute NACA 0012	52
FIG. (18) Local Nusselt Number(l) on 0 Minute NACA 0012	53
FIG. (19) 5 Minute Glaze Ice Profile on NACA 0012	53
FIG. (20a) Local Nusselt Number(C) on 0 and 5 Min. NACA 0012	54
FIG. (20b) Local Nusselt Number(l) on 0 and 5 Min. NACA 0012	54
FIG. (21) Velocity Field Around 5 Minute NACA 0012	55

LIST OF TABLES

	PAGE
Table(1) Coordinates and Thermocouple Locations of 2 Minute Model on a Cylinder	56
Table(2) Coordinates and Thermocouple Locations of 5 Minute Model on Cylinder	57
Table(3) Coordinates and Thermocouple Locations of 15 Minute Model on Cylinder	58
Table(4) Fourier Coefficients for 15 Minute Rough Model	59
Table(5) Fourier Coefficients for 15 Minute Rough Skin	60
Table(6) Coordinates and Thermocouple Locations of 5 Minute Model on NACA 0012 Airfoil	61

Accession For	
NTIS GRA&I	<input checked="" type="checkbox"/>
DTIC TAB	<input type="checkbox"/>
Unannounced	<input type="checkbox"/>
Justification	
By _____	
Distribution/ _____	
Availability Codes	
Avail and/or	
Dist	Special
A-1	



NOMENCLATURE

A	surface area
a	Fourier coefficient
b	Fourier coefficient
B	blockage ratio
c	Fourier coefficient
C	chord of airfoil
d	Fourier coefficient
d	droplet diameter
D	diameter of cylinder
f	frequency
h	heat transfer coefficient
I	current (amperes)
k	absolute roughness
k_s	sand grain roughness
K	thermal conductivity
kph	kilometers per hour
l	distance along surface from forward stagnation
L	half signal interval
m	spatial frequency
n	spatial frequency
Nu_D	Nusselt number hD/k
Q	heat flux
R	radius
Re_D	Reynolds number $\rho UD/\mu$
T	temperature
U	velocity
v_*	friction velocity $\sqrt{\tau^*/\rho}$
V	voltage (Volts)
w	liquid water content
W	Watts
X	cartesian
Y	cartesian
Z	cartesian
Θ	angle in radians measured from positive X axis
ψ	angle measured from forward plane of symmetry
α	angle of attack
ρ	density
μ	viscosity
τ	time
τ^*	turbulent shearing stress
λ	wavelength, width between roughness elements

Subscripts

w	wall
∞	ambient

CHAPTER 1

INTRODUCTION

In recent years, the problem of ice formation on aircraft has received considerable attention because of its influence on military aircraft capabilities. Military aircraft and helicopters may be required to operate under icing conditions which would effect their performance, maneuverability and impair the mechanical integrity of unprotected engines. Two symposia have been held exclusively on the ice accretion processes and papers presented in these meetings along with discussion have been published in two AGARD reports^{1,2}. In addition, a special session on icing phenomena was arranged by the American Institute of Aeronautics and Astronautics at its Aerospace Sciences Meeting in January 1981³.

- Ice formation poses a hazard to flight in that it alters the aerodynamic characteristics of lifting surfaces, reducing the maximum lift and sharply increasing the drag^{4,5,6}. The horn like accretions forming on the leading edge act as spoilers or as large roughnesses^{7,8}, inducing severe adverse pressure gradients which trigger the formation of small zones of separated flow which at higher angles of attack may lead to massive separation and stall. For engine installations which require inlet ducting, ingested ice can accumulate, melt and refreeze to present a serious problem^{6,9}. In addition the ice formation may lead to control problems and, if it sloughs off, damage structures downstream. The above situations can cause serious problems for military aircraft or missiles flying over the North Atlantic and North Sea. In Europe in winter it is possible to have the proper weather conditions for ice formation up to 30 percent of the time¹⁰. The ice accretion

process is of prime interest in aircraft design. In order to develop and then certify certain protection systems¹¹⁻¹⁶, it is necessary to be able to test engine intakes, aerofoils in simulated icing conditions.

ICE FORMATION

Ice accretion is dependent upon^{17,18},

- (a) ambient temperature (T_{∞})
- (b) liquid water content w
- (c) droplet diameter d
- (d) flight velocity (U_{∞})
- (e) aerofoil geometry $y=f(x)$
- (f) icing time t .

The shape of the ice accretion depends on airfoil shape, leading edge radius, camber, and angle of attack α ¹⁹. Depending on the above parameters, different kinds of ice form^{4,20}.

(1) Glaze ice forms with air temperature a little below 0°C, and when the liquid water content is high. The water droplets do not freeze immediately after impingement but run first on the profile upward or downward from the stagnation point before freezing. The result is a deposit of ice with two horn like protrusions, Fig (1), and normally is transparent and harder than rime ice. The horn shaped structure is characteristic for glaze ice and the major protrusions occur in the regions of maximum heat transfer. These protrusions become relatively large compared to the boundary layer thickness effecting the flow and heat transfer characteristics of the surface. Since the quantity of water is mostly large, ice formation is correspondingly heavy and adheres tightly to the surface.

(2) Rime ice forms at lower temperatures and mostly low liquid water content in the clouds. The lower the temperature and liquid water content, the more difficult it is for the droplets to flow together. Upon impingement on the airfoil surfaces, they are only slightly deformed and freeze to almost spherical grains of ice, resulting in a milky white, porous structure.

(3) Intermediate or mixed ice may apart from the two main types, glaze and rime ice, cover a broad spectrum. Depending on conditions a composite or laminate structure may evolve, for example, glaze ice may follow rime ice or vice versa.

(4) Hoarfrost is possible in clear and cloud free air when an aircraft flies from a layer of cold air into another though cloudfree but warmer and moist layer of air, thus cooling down the ambient air within the influence of its surface. As soon as this air is cooled to below 0°C, hoarfrost occurs. It has a white feathery, crystalline appearance.

Extensive experiments have been performed on airfoils to measure and predict static and dynamic pressure measurements²¹, aerodynamic lift and drag characteristics⁶, and the droplet size and trajectories^{17,22}, however, very little heat transfer data is available. The thermodynamic conditions for either rime or glaze ice to form on structures are well understood. Several empirical theories^{6,17,19} have been developed which can predict the amount of ice formed. However, they rely on questionable application of heat transfer results. Ice accretion is dependent on the rate of solidification which is in turn dependent on the rate at which the heat of fusion may be released to the surroundings, i.e. the ability of the flowfield to remove heat, from which we deduce that one of the significant parameters in the ice accretion process is the local convective heat transfer coefficient. Knowledge of the

thermal boundary layer, determination of the local heat transfer coefficient at various Reynolds numbers will assist in predicting local ice growth rates. The primary objective of this study is to measure the local heat transfer coefficient.

Small objects accrete ice more rapidly than large ones. All the harmful effects of ice accretion namely, drag rise, torque rise, power loss, lift deterioration, stall angle decrease, and stall speed increase, occur faster and are more perilous on small unprotected aircraft. Hence an obvious choice would be to choose a geometry which would be subjected to the most severe conditions. The NACA 0012 helicopter rotor was selected as an appropriate test specimen. Prior to investigating thermal characteristics over airfoils, experiments were performed on a cylinder, a problem which is well documented in literature²³. The nose of an airfoil can be approximated to the stagnation region of a cylinder. Ice accretion being a problem plaguing mostly the leading edge, a cylinder serves as a very good approximation. Changes in the aerodynamic performance are not only influenced by the amount of ice accumulated, but more significantly, determined by its shape. Accordingly glaze ice profiles are selected for this study.

EXPERIMENTAL PROGRAM

This investigation was accomplished over a series of steps. The second chapter discusses the heat transfer problem of ice accretion and experimental methods of determining the local heat transfer coefficient. Velocity profiles along with heat transfer results are presented for ice accretions on a cylinder. The ice accretion is not of smooth geometry, thus the surface undulations have profound effects on the structure and behaviour of the velocity

and thermal boundary layers. In general, the heat transfer coefficient is greater in a turbulent boundary layer influenced by roughness than in a smooth wall layer at the same flow conditions. This enhancement of heat transfer because of the roughness effects must be understood and accounted for. Chapter 3 details a Fourier analysis approach to precisely define a surface so as to isolate profile components which characterize the flowfield around a rough 15 minute glaze ice on a cylinder. Finally, in Chapter 4 heat transfer and velocity profile results are presented on the NACA 0012 airfoil without and with a glaze ice accretion at angles of attack ranging from $\alpha=0^\circ$ to 8° , followed by concluding remarks.

CHAPTER 2

The starting point of atmospheric ice accretion are the clouds and their contents of supercooled water droplets, ice crystals, or a mixture of both. Because supercooled liquid is in a thermodynamic state of metastable equilibrium, a significant physical disturbance such as flying aircraft causes the droplets to rapidly change to the stable equilibrium state of ice on the impinging surfaces. The ice accretion process takes place through a series of concurrently occurring energy transfer mechanisms^{17,24}, simply stated as:

- (a) convective heat losses
- (b) latent heat gain
- (c) heat loss due to evaporation and sublimation
- (d) heat gain due to kinetic energy.

For an adiabatic wing the energy balance of the above processes must be dissipated into the ambient through convection. Owing to the speed of most aircraft the heat transfer process can be considered to be forced convective.

EXPERIMENTAL METHODS

(1) Thin skin transient method: since the local heat flux varies over the surface for an isothermal boundary condition, the surface material must have the thermal capability of equilibrating the temperature within it, ie., it must ideally have an infinite thermal conductivity. The above conditions not being met conduction effects come into play, necessitating a fast and accurate data acquisition system²⁵.

(2) Sublimation method: employing materials such as Naphthalene, Dry Ice etc. which sublimate readily, the heat transfer coefficient can be determined by the loss of weight, however, due to the complex geometry of the surface, evaluation of local mass transfer rates can become cumbersome.

(3) The steady state heat flux method

Newton's Law of Cooling²⁶,

$$Q = hA (T_w - T_\infty) \quad \text{Watts} \quad (1)$$

defines the convective heat flux between a fluid at temperature T_∞ in contact with a surface at temperature T_w . The proportionality constant h ($\text{W/m}^2\text{K}$) is referred to as the heat transfer coefficient. It depends on the conditions within the boundary layer, which are a function of the surface geometry, the nature of the fluid motion and fluid thermodynamic and transport properties^{26,27}. In applying this law to our problem of glaze ice accretion, a case in which we have mass transfer of water from the fluid to the body surface by freezing due to convective heat loss, we can assume an isothermal surface at a temperature equal to that of the freezing point of water. Lack of experimental facilities limit an exact simulation, with respect to mass transfer of water droplets from air to surface, which are assumed to be not sufficiently numerous to perturb the flow. As ice accumulation builds on the leading edge of an aerofoil, the flowfield must slowly adjust to the new boundary conditions imposed by the change in shape. This change in the aerofoil shape, and the resulting change in the flowfield, will also alter impingement rates on the surface. Thus the ice accretion process is also a function of time and must be modelled accordingly. One method of modelling the effect of time is a time stepping approach, assuming ice accretion can be broken down into a series of steady state processes. Hence, if we consider the glaze ice at any instant in time, and assume no further ice accretion, then the geometry is fixed. The heat transfer coefficient can then be acquired experimentally as long as one can reproduce the geometry and flow

conditions (Reynolds and Prandtl number), and provide an isothermal surface to ensure a similar thermal boundary layer. If the above conditions are satisfied, the heat transfer coefficient can be evaluated from knowledge of the local heat flux and respective temperatures required by Newton's Law of Cooling.

APPARATUS

The experiment was conducted in the subsonic wind tunnel facility in the Department of Mechanical Engineering at the University of Kentucky. The induced flow wind tunnel is equipped with a 50 kW axial fan and has a 4.8 mm honeycomb, 102 mm in depth, for straightening the flow, at the upstream end of the plenum chamber. The 508 mm x 711 mm x 1220 mm test section has three sides made of plexiglass for use in flow visualization with ports provided in the sides for taking velocity measurements using a hot film probe over a three dimensional grid. Velocities up to 160 mph can normally be obtained in this section.

In these experiments, the problem of maintaining a uniform temperature on the surface is solved by using many independent narrow strips of Minco therмоfoil heaters, 5.9 mm x 175 mm x 0.3 mm, glued on, with the long sides touching, to the white pine wooden body of the model to form the surface of the glaze ice (see Fig (2)). The temperature of the surface is measured using thermocouples. Hence, if the model is made of insulating material, (white pine used in these experiments), most of the heat must be dissipated directly into the fluid medium. The electrical energy input is converted into thermal energy in the resistance of the heaters, which essentially is our required heat flux.

$$Q = V \times I \quad \text{Watts}$$

(2)

This wooden model is then attached to a 50.8 mm, thin walled (1.7 mm) brass cylinder, or airfoil as the case may be, closed at both ends to minimize heat losses due to free convection from within and held vertically and clamped firmly at its ends. The model is aligned with the direction of the flow using two static pressure ports equally spaced from a reference stagnation point. Each heater has an individual a.c. power supply. The voltage across each heater is measured using a HP3455A digital voltmeter. The current through each heater is measured by a FLUKE 8600A digital multimeter. A bank of quick disconnects makes it possible to connect the one ammeter in series with any heater circuit, one at a time. Each heater has a 0.02 mm inconel element which has a negligible temperature coefficient of resistance in the temperature range of interest.

The temperature of each individual heater is monitored using three OMEGA 1 mm Copper-Constantan thermocouples placed equidistantly along the length. This provides not only a temperature distribution on the surface but also acts as a backup feature in case any one thermocouple malfunctions. This latter precaution is necessary since the temperature of the entire surface has to be maintained in an isothermal state within experimental limits. The thermocouple junctions are affixed to the top of the heater surface using a highly conductive Omega 101 epoxy as a heat sink. Thermocouples are also placed at the junction of the ice profile with the cylinder in order to measure the base cylinder temperature from which an estimate of the conductive heat losses through the wooden model can be calculated. Less than 5% of the heat generated at the surface was conducted away from the surface. The whole assembly is finally covered with adhesive backed, thin (0.07 mm) aluminum foil to give a smooth and continuous surface. Because the foil is thin, it is

assumed that it does not affect the heat transfer into the air stream. Also, the low emissivity of aluminum reduces heat losses due to radiation (less than 1.2%). Calibrated Omega electronic ice points are used in conjunction with the thermocouples and these voltages are read and recorded using a HP 3467A logging multimeter. Electrical access to any heater or thermocouple is facilitated through a bank of scanners. The free stream temperature T_∞ is measured by a separate thermocouple mounted inside the test section.

The velocity is measured using a TSI 1210-20 single hot film sensor controlled by a TSI 1050 series constant temperature anemometer. The linearized signal is measured by a HP 3455a digital voltmeter, a DISA 55D35 RMS voltmeter provides the turbulence intensity. The linear response of the anemometer was checked using a nozzle with a 3.41:1 contraction ratio, a stilling chamber and a flow straightener. The nozzle upstream pressure was measured by a Miriam Micromanometer to within ± 0.025 mm of water. The setup was designed by Abdelghany²⁸ to supply a low turbulence air jet, free of swirl.

EXPERIMENTAL PROCEDURE

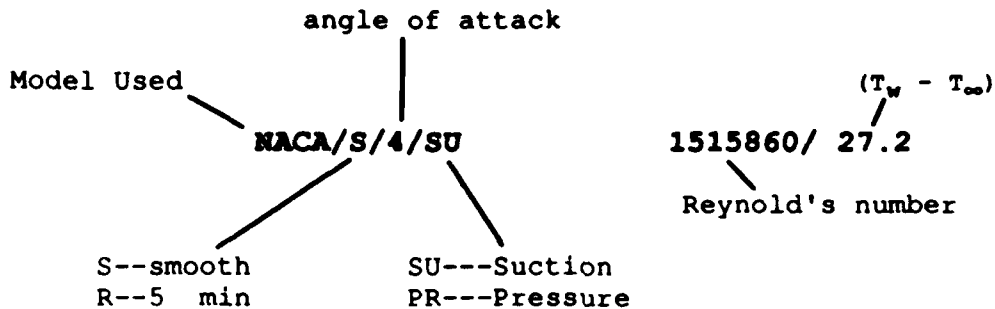
The wind tunnel was allowed to run for 5-10 minutes in order to attain steady flow and temperature conditions. The velocity was set so as to obtain a pre-determined Reynolds number. The power to the individually controlled heaters was switched on and the thermocouple temperatures were continuously monitored, until a constant temperature was attained over the surface. Once steady state conditions were reached, the voltage across, the current through, and the thermocouple voltages on each heater were noted. Finally, the free stream temperature and velocity were recorded.

The calibration of the hot wire indicates a correlation coefficient of 0.998 or better. Calibrations were performed before each experiment to take care of changes in temperature and weather. Using the Hot Film probe, a profile of the velocities within the test section was obtained over a 16x27 grid. The velocity was observed to be uniform over the test section. The maximum intensity of turbulence in the central region was of the order of 0.5%. As stated earlier, the models are equipped with three sets of thermocouples, top, middle and bottom rows respectively. In performing the experiment it is necessary to select one of the rows which will determine the constant surface temperature condition (generally the choice would be the middle row from symmetry considerations). This is necessary since once the power to a heater is set with respect to one of its thermocouples, then the temperature indicated by the remaining two is automatically fixed as no other control is available to change their output without changing the initial setting. Hence, at steady state, we will have a band around the model in which the temperature is very much constant. The other regions may have slight temperature variations. The authors used this isothermal band for the calculation of the necessary parameters of this study. Note that this assumption is valid since the temperature coefficient of resistance of the thermofoil heater is negligible in the temperature range of interest.

The experimental setup at the University of Kentucky was first tested to obtain reliable measured results. To do this an initial experiment was performed to measure the local heat transfer coefficient on a two inch cylinder using the steady state heat flux method. The data obtained agrees well with published results^{29,23} (see Fig (3)). Plaster casts of ice growth on a 50.8 mm cylinder were obtained from experiments conducted in the icing research

tunnel at NASA, Lewis. The profiles obtained were smoothed and coordinates of the same were provided to the authors by Shaw³⁰. A selected set of 2, 5 and 15 minute smooth glaze ice profiles were prepared as described in the section "Apparatus" in Chapter 2. The shapes of the growth of glaze ice on a cylinder (smoothed profiles), are shown in Fig. (1).

Explanation of the legends in the figures is as follows,



For all cases in this study the Nusselt and Reynold's numbers were calculated using the Film temperature ($T_w - T_\infty$) and a characteristic length, the diameter D or chord C.

2 MINUTE GLAZE ICE ON A CIRCULAR CYLINDER

This protrusion covers 116° of angular surface or a total non-dimensional length (1/D) of 1.35. The blockage ratio for the model is equal to 0.078. The maximum variation in temperature is 1.0% over the entire central band at a surface temperature of 48°C. The mean of the local heat transfer coefficient of symmetric points about the forward stagnation (location $\psi=0^\circ$), was taken. This procedure showed a ± 47 variation in the Nu_D number and a ± 0.12 variation in the $Nu_D/\sqrt{Re_D}$ at any location. Radiation losses were minimal at 0.3% and conduction losses were measured and assessed to be not greater than 5% which occurred at the junction of the ice shape with the cylinder.

Fig (4) is a plot of $Nu_D/\sqrt{Re_D}$ vs angle which compares the results with those of Van Fossen³¹ and Arimilli²⁹. This shows that the authors' data compare well with that of Van Fossen³¹ over most of the region. We also find much higher values at the junction of the ice with the cylinder in the downstream end. This may be due to the higher curvature in this section of the model. Arimilli²⁹ shows the same qualitative trend but is lower by around 13% on the average with the authors' data as the base.

5 MINUTE GLAEE ICE ON A CIRCULAR CYLINDER

This ice shape covers 122° of angular surface or a total non-dimensional length (l/D) of 1.89. The blockage ratio for this model is equal to 0.088. The maximum temperature variation is around 1.0% over the entire central band at a surface temperature of 52°C. The mean of the local heat transfer coefficient of symmetric points about the forward stagnation was taken. This procedure shows on the average a ± 14 variation in the Nu_D number and a ± 0.04 variation in the $Nu_D/\sqrt{Re_D}$ at any point. Radiation losses were less than 0.3% and conduction losses measured did not exceed 3% which occurred at the junction of the ice shape with the cylinder.

The data of Van Fossen³¹, Arimilli²⁹ and the authors are compared in Fig (5). This shows very good agreement between Van Fossen³¹ and the present data. The authors' show much higher values at the junction of the ice with the cylinder in the downstream end. This again may be due to the higher curvature in this section of the model. Arimilli²⁹ shows the same qualitative trend but is lower by about a maximum of 75% with the present data as the base.

15 MINUTE GLAZE ICE ON A CIRCULAR CYLINDER

This model covers 125° of angular surface or a total non-dimensional length (l/D) of 4.2. The blockage ratio for this model is equal to 0.132. The maximum temperature variation is around 1% over the entire band at a surface temperature of 55°C . The mean of the local heat transfer coefficient at symmetric points about the forward stagnation was taken. This procedure shows on the average a $\pm 4\%$ variation in the Nu_D number and a ± 0.12 variation in the $Nu_D/\sqrt{Re_D}$ at any location. Radiation losses were less than 1.2% and conduction losses were measured and assessed to be not greater than 4% which occurred at the junction of the ice shape with the cylinder.

Fig (6) shows a comparison of the data with published results from Van Fossen³¹ and Arimilli²⁹. The authors data compare in trend with those of Van Fossen³¹ over most of the region showing values lower than those of Van Fossen³¹ at times by up to 27% based on the authors' data. Past the horn ($\psi=35^\circ$) of the protrusion and downstream, the heat transfer coefficient is observed to follow a wave like function. A numerical flow study on the same profile performed by Calarese³² lends credence to this behaviour. The flow going around the horn, encounters downstream regions of separation and reattachment which would cause sudden changes in the thermal boundary layer and hence, the undulating form of the local heat transfer coefficient. Arimilli²⁹ follows the trend up to the stagnation point at the horn but falls off rapidly in magnitude later downstream.

A study of the velocity field, ahead of the 15 minute model, in a three-dimensional grid between 76 and 140 mm upstream from the center of the cylinder is shown in Fig (7). This is a contour plot in the XZ and XY planes of

the non-dimensional velocity based on the maximum velocity in the Y direction, ie. the direction of flow. The velocity profile in the region of interest is noted to be uniform and symmetric about the longitudinal axis of the model. A large stagnation zone exists upstream of the profile where velocities drop to less than 40% of the free stream up to 2 diameters away. In the case of the 15 minute profile the stagnation zone extends up to approximately 305 mm (6 diameters) upstream from the center of the cylinder. It is also observed that the flows in both the XZ and XY planes are not exactly symmetric and may be the cause of asymmetries in the boundary layer flow leading to the variation in the heat transfer coefficients measured at locations symmetric about the forward stagnation.

The comparison of the local heat transfer rates for the three profiles shown in Fig (1) is provided in Fig (8). It is observed that as the ice grows on the cylinder the heat transfer coefficient at any region decreases. This can be explained by noting that as the ice grows it takes up a two-dimensional concave profile in the forward stagnation zone. This tends to enlarge the upstream stagnation zone, which may extend many diameters ahead. All this results in slower velocity and thicker thermal boundary layers which results in the heat transfer coefficient being lowered.

Calculations were done to correlate some characteristic dimension of the profile, which includes ice growth, with the Nusselt number. When the Nusselt number is based on the maximum width of the profile subtended by the flow, the data from the different ice profiles tend to coalesce. A better correlation also exists between $Nu_D/\sqrt{Re_D}$ and angle than between $Nu_D/\sqrt{Re_D}$ and 1/D. Coordinates and thermocouple locations of the 2, 5, and 15 minute models are provided in Tables (1,2,3).

CHAPTER 3

Surfaces produced by various processes exhibit differences in texture. These differences make it possible for turned, polished, milled or ground surfaces to be easily identified. From the fluid mechanics and heat transfer point of view the variations in the surface texture influence the flowfield, thereby, increasing or decreasing drag, lift and the ability to transfer heat which may under certain conditions be critical.

The precise definition and measurement of surface-texture which is irregular in shape and which does not lend itself to direct measurement can become very complex. Hence, there is a need for improved methods of determining, designating and controlling the surface texture. Texture can be qualitatively described by its coarseness, in that burlap is more coarse than silk. The coarseness index is related to the spatial repetition period of the local structure. A large period implies a coarse texture and a small period, a fine texture. This perceptual coarseness index is clearly not sufficient as a quantitative measure of texture.

ROUGHNESS DEFINITION

The classical definition of roughness strives to describe surface irregularities quantitatively and qualitatively in a number of ways³³, for instance:

- (a) The roughness-height index value is a number which equals the arithmetic average deviation of the minute surface irregularities from a hypothetical perfect surface,
- (b) waviness refers to the secondary irregularities upon which roughness is superimposed, which is of significantly longer wavelength.
- It is defined as the maximum peak to valley distance.
- (c) Lay refers to the

direction of the predominantly visible surface-roughness pattern. The standards are not concerned with other surface qualities such as hardness and microstructure.

If the surface is composed of a combination of a number of elementary surfaces superimposed on one another, then a two-dimensional Fourier analysis can be easily applied. Several studies³⁴⁻³⁶ have considered textural analysis in terms of the Fourier spectrum of a region. Since the degree of texture coarseness is proportional to spatial period, a region of coarse texture should have its Fourier spectral energy concentrated at low spatial frequencies. Conversely, regions of fine texture should exhibit a concentration of spectral energy at high spatial frequencies. Thus, roughness description may be enhanced using those superior techniques borrowed from more established disciplines.

THEORY

A Fourier series,

$$f(x) = \frac{1}{2}a_0 + \sum_{n=1}^{\infty} a_n \cos \frac{n\pi x}{L} + \sum_{n=1}^{\infty} b_n \sin \frac{n\pi x}{L} \quad (3)$$

is a representation of a function $f(x)$ as a linear combination of all those cosine and sine functions in an interval $(-L, L)$ which have the same period³⁷. Fourier series in this sense can be used for analyzing oscillations or waveforms periodic in space. The Fourier series may also be used to represent a function which is not periodic, but instead is defined in the first place only in a restricted interval. A two-dimensional Fourier transform represents a rotation of coordinates of a two-dimensional coordinate system into a new set of orthogonal coordinates also of two dimensions. Hence, there exists

a coordinate rotation which causes certain dimensions to become more relevant than others, thereby permitting the surface to be categorized with the aid of fewer but more relevant dimensions.

Application of Fourier analysis to define such surface profiles provides a two fold advantage: (a) The large amount of discrete surface coordinate data is described using mathematical relations which are simple and require far less memory, allowing a sizable data reduction^{36,38} and (b), the amplitude and frequency of the sinusoidal functions are analogous to the properties of the classical definition of roughness.

The term frequency is applied to a set of sinusoidal functions whose zero crossings are uniformly spaced over an interval. The parameter n that belongs to sets of functions of the form $\cos(n\pi x/L)$ and $\sin(n\pi x/L)$, as in Equation (3), is interpreted as the number of complete cycles generated by a sinusoidal function per unit length $2L$.

Given a surface $h(x,y)$, a two dimensional Fourier transform

$$H(m,n) = \iint_{-\infty}^{\infty} h(x,y) e^{-j(mx+ny)} dx dy \quad (4)$$

decomposes the two dimensional function into an infinite set of coefficients of two dimensional orthogonal complex trigonometric waveforms given by the Fourier kernel $\exp(-j(mx+ny))$. The inverse Fourier transform is then given by,

$$h(x,y) = \iint_{-\infty}^{\infty} H(m,n) e^{j(mx+ny)} dm dn \quad (5)$$

The terms m and n are called the spatial frequencies of the image in analogy with time series analysis. If a signal is defined over a finite interval $2L$, then its Fourier transform is exactly specified by the Fourier series at a set of equally spaced points on the frequency axis. The distance³⁷ between these points of specification is $1/2L$. When Fourier analysis is applied, the origin or zero spatial frequency term appears in the corner of the transform plane. For display purposes it is shifted to the center of the transform domain (see Fig (9b)). The two-dimensional Fourier transform of an image is essentially a Fourier series representation of a two dimensional field.

The most basic of all surface features is the measure of surface amplitude. A surface array is considered to be a rectangular array of $N \times M$ altitude samples described by the function $h(x, y)$ over the surface coordinates (x, y) . The coefficients of the two-dimensional Fourier transform, $H(m, n)$, specify the amplitude of the basis functions such that the weighted sum of the basis functions is identical to the image. Then the two-dimensional discrete forward transform of the surface array, $H(m, n)$, itself defined on a rectangular array of $N \times M$ points, may be expressed as,

$$H(m, n) = \frac{1}{\sqrt{MN}} \sum_{x=-M/2}^{M/2-1} \sum_{y=-N/2}^{N/2-1} h(x, y) e^{-j(mx+ny)} \quad (6)$$

Parseval's theorem being satisfied, each spectral component in the transform domain corresponds to the amount of energy of that spectral orthogonal function within the original surface⁴⁰.

The $h(x, y)$ function describes a surface having $N \times M$ components, and the FFT $H(m, n)$, is a complex function containing $2 \times N \times M$ components. Owing to the fact that $h(x, y)$ is a real positive function, $H(m, n)$ displays a property of conju-

gate symmetry, hence, it is necessary to obtain only one half of the transform plane, ie., the surface can be described by NxM components of the FFT^{39,40}. The Fourier analysis is implemented using a fast Fourier transform(FFT) algorithm^{40,41}. The transform being symmetric and separable, the FFT is applied on the two-dimensional surface in two sequential steps of one dimensional transforms^{39,40}. Then the surface can be written in the Fourier series representation as,

$$h(x, y) = a_0 + \sum_{m=1}^{M/2} a_m \cos \frac{m\pi x}{L_x} + \sum_{m=1}^{M/2} b_m \sin \frac{m\pi x}{L_x} + \sum_{n=1}^{N/2} c_n \cos \frac{n\pi y}{L_y} + \sum_{n=1}^{N/2} d_n \sin \frac{n\pi y}{L_y} \quad (7)$$

where,

$$\lambda_m = 2L_x/m$$

$$\lambda_n = 2L_y/n$$

$$H(m, 0) = a_m/2 + i b_m/2 \quad m=1, M$$

$$H(0, n) = c_n/2 + i d_n/2 \quad n=1, N$$

are the complex coefficients obtained from the FFT at the points m, n on the principal axis of the transform plane. The coefficients h(m, n) at locations other than the principal axis are not being considered in this study as they define functions which do not contribute to the definition of roughness.

For example consider the function h(x, y) defined as follows,

$$h(x, y) = 0.2 \cos 2\pi 17x + 0.1 \sin 2\pi 6y \quad (8)$$

This corresponds to a two dimensional surface, as shown in Fig (9a), composed of the sum of sinusoidal surfaces of frequency 17 in the X direction and of frequency 6 in the Y direction. If a two dimensional Fourier transform is performed on this surface, the resulting spectrum contains peaks at locations corresponding to the respective frequencies of the surface. The sum of the

absolute value of the peaks, for the same frequency, gives the amplitude of the function. This is confirmed from Fig (9b). In order to perform the Fourier transform the surface must be discretized into a NxM grid, where N and M must satisfy the Sampling theorem⁴⁰,

$$N \text{ and } M \geq 4BL \quad (9)$$

where,

N, M-----number of divisions

B-----Bandwidth or maximum frequency

L-----half signal interval

in order to recover the function wholly in the transform domain. Owing to the discrete and finite nature of the FFT employed, the exact function is not recovered in the transform domain, as distribution of some of the energy of the original function over other frequencies occurs. This may be reduced by applying windowing techniques, or by using larger grids.

In the present example a 64x32 grid was used. The function recovered from the Fourier analysis can be written in the form,

$$h(x,y) = 0.18\cos 2\pi 17x + 0.092\sin 2\pi 6y \quad (8a)$$

which has a relative error in magnitude of between 8% to 10% based on the original function. Doubling the grid to 128x64 gives,

$$h(x,y) = 0.196\cos 2\pi 17x + 0.098\sin 2\pi 6y \quad (8b)$$

which has a relative error of 2%, increasing the accuracy by a factor of four.

Having confirmed the ability of the Fourier analysis to extract pertinent information in two-dimensional surfaces, the next step was to apply the technique to the 15 minute glaze ice surface.

FABRICATION

Fig (10) shows the rough surface profile of a fifteen minute glaze ice accretion on a 50.8 mm cylinder. A plaster cast, one inch long in the axial direction of the cylinder, was obtained from Shaw³⁰, from experiments conducted in the icing research tunnel at NASA, Lewis³¹. The icing conditions were as follows:

Liquid water content $w = 2.1 \text{ g/m}^3$

average droplet size $d = 20 \mu\text{m}$

$T_{\infty} = -7.8 \text{ deg C}$

$U_{\infty} = 208 \text{ kph}$

Experiments were performed earlier by the authors (see Chapter 2) on smooth 15 minute glaze ice models. Since the geometry of the smooth model, excluding the roughness of the surface, was similar in all respects to the actual glaze ice profile³¹ it was decided to use these smooth models with all the heaters and thermocouples attached as a base for the actual rough models (see Fig (11)). This saved considerable time in the laying out of the heaters, thermocouples and the associated electrical circuit connections, (see section on HEAT TRANSFER CHARACTERISTICS in this chapter).

A number of methods of fabrication were considered. Two methods, namely, the lost wax method and a three step process were tried. The latter was considered to be more practical and so was adopted and will be described here.

(a) A master mold of one of the originals³¹ was first made by pouring Kerr Permalastic impression material into a one-inch-deep thin walled plastic beaker in which one of the original 15 minute cast was firmly positioned. The original cast was of approximately one inch axial length, hence, the shallow

beaker. Kerr Permalastic is a fast setting (10 minutes), two part rubber epoxy which will flow into and conform to complex surface undulations with tolerable (less than 5%) shrinkage on setting. Being rubber it is pliable, making it easy to remove the rubber mold from the cast without destroying either. Thus, the cast is re-usable. Once the rubber mold was made a number of replicas of the original cast were made using Microstone Whip Mix, a quick setting dental plaster. These replicas were then joined end to end in order to get a model which was approximately 20 inches in length.

(b) Having made the 20 inch cast, the next step is to somehow transfer or copy the surface configuration onto the smooth ice surface. Since the smooth ice shape has similar dimensions as the newly cast piece a careful transfer of the surface profile would produce a final model true to the original. The surface of the 20 inch plaster cast, prepared in step (a), is wetted with water and a 0.4 inch thick layer of Kerr Permalastic is evenly poured on the surface. On setting, the thin layer of water on the cast prevents any adhesion of the rubber to the cast and, thereby, assists in the easy removal of the resulting rubber sheet containing a 1:1 imprint of the rough surface.

(c) Since the rough surface is to be reproduced on the smooth surface above the heaters and thermocouples, it is necessary to make the rough skin-like surface of a high thermally conductive and adhesive material. A suitable choice was found in Omega 101 two part epoxy adhesive.

Thermal Conductivity K=1.04 w/m.^oK

Coefft. thermal Exp. 3.6x10⁻⁵ cm/cm/^oC

Continuous operating temperature = 135 ^oC

A thin layer of approximately 0.25 inch of the mixed Omega 101 epoxy was evenly spread on the surface of the smooth model. The rubber sheet prepared

in step (b) was sprayed with a very thin oil (WD-40), which prevents the epoxy from sticking to it. Making sure that no air bubbles were trapped inside, the rubber sheet was then pressed lightly on to the epoxy coated surface. The epoxy flows into and sets in the configuration provided by the rubber surface mold. The rubber sheet is peeled off, leaving the cured epoxy skin implanted with the rough surface profile. This is finally coated with a 'flat black' paint of about 98% emittance.

Surface coordinates were obtained by mounting the model on a vertical semi-universal milling machine with a three degree freedom of motion table. Using a micrometer gauge accurate to a thousandth of an inch, with a feeler of tip radius 0.002 inch, the coordinates of the surface of the 15 minute glaze ice were obtained over 1 inch length in the vertical direction (Z-axis) on a grid spacing of 0.1 inch in each direction. Thus surface coordinates were obtained over a 11x104 grid. A view of the various section profiles is provided in Fig (10).

FOURIER ANALYSIS

The Fourier analysis was first performed on the whole profile of the 15 minute glaze ice. This can be considered as a large roughness element placed on the cylinder in cross flow.

The 15 minute glaze ice surface in the Cartesian coordinate system is a double valued function of x , as can be noted from Fig (10). This poses problems in interpreting the Fourier coefficients. This problem can be circumvented by transforming the data to the cylindrical coordinate system with angle Θ , as the independent variable. Here Θ is the angle measured in radians from the positive direction of the X axis in the counter-clockwise direction.

tion. The 104x11 surface grid was converted to cylindrical coordinates and further grids of 256x32 and 512x64 obtained with the help of two-dimensional B-spline interpolation routines. The increase in the grid is necessary to satisfy the sampling theorem, thus making certain that all possible frequency components are extracted. A three-dimensional plot of the FFT is shown in Fig (12). The coefficients of the function,

$$R(\theta, z) = a_0 + \sum_{m=1}^{M/2} a_m \cos \frac{m\pi\theta}{L_\theta} + \sum_{m=1}^{M/2} b_m \sin \frac{m\pi\theta}{L_\theta} + \sum_{n=1}^{N/2} c_n \cos \frac{n\pi z}{L_z} + \sum_{n=1}^{N/2} d_n \sin \frac{n\pi z}{L_z} \quad (10)$$

as modified from Equation (7), for a grid of 256x32, in the θ and z directions are provided in Table (4). From our analysis it was ascertained that a 256x32 grid more than suffices the requirements of the sampling theorem. Further increase to 512x64 produces no change in the FFT. From Fig (12) we note that for $\lambda_\theta < 0.065$ radian in the θ direction and $\lambda_z < 0.11$ inch in the z direction the FFT coefficients vanish, i.e. they are less than 0.002 inch, the tip radius of the measuring probe. The number of data points to completely define the surface is 128. Compared to 8192 data points of the initial grid, this translates to a data reduction by a factor of 64.

In performing the Fourier analysis the appropriate surface must be selected. The whole ice shape can be considered as a large roughness element on the cylinder, or, since we are also interested in the local heat transfer coefficient which is dependent on the characteristics of the local and neighboring surface geometry and its corresponding momentum and thermal boundary layer²³, a more detailed description of the local rough surface may be required.

In order to acquire the aforementioned, the rough fifteen minute glaze ice profile can be considered to constitute a 15 minute smooth profile on which is laid a thin "rough skin" (see Fig (10)). It then becomes necessary to perform the Fourier analysis on the hypothetical rough skin which covers the smooth ice shape. The coordinates of this skin are mathematically obtained by subtracting the smooth profile from the rough profile. Using a surface spline fitting algorithm the amplitude of the rough surface from the smooth glaze ice is determined, the profiles are shown in Fig (13a,b). One observes from experiments that such profiles are characteristic of glaze ice formation under conditions similar to those specified in "Fabrication". Knowledge of the Fourier coefficients for the above skin can then be implemented in laying skins on other surfaces which may be exposed to similar ambient conditions.

The skin profile coordinates were calculated over a 157x11 surface grid which was further divided into grids of 256x32 and 512x64 using methods described earlier in order to satisfy the sampling theorem (see Equation (9)). A three-dimensional plot of the FFT is shown in Fig (13c). An analysis of the spectrum ascertained that a 256x32 grid adequately satisfies the sampling theorem. Further increase to 512x64 produces no change in the FFT. From Fig (13c) we note that for $\lambda_x < 0.23$ inch in the X direction and $\lambda_y < 0.17$ inch in the Y direction the FFT coefficients vanish. The coefficients of Equation (7) obtained from the above analysis are provided in Table (5). The number of data points to completely define the surface is 107. Compared to 8192 data points of the initial grid, this translates to a data reduction by a factor of 76.

ROUGHNESS DESCRIPTION

Consider ice accretion on a cylinder. From Fig (8) we note that within the forward stagnation zone, the Nusselt number decreases at any particular angle as the ice grows with time. At the tip of the horn, however, the Nusselt number remains approximately the same. Flowfield velocity studies show that as the ice grows, the stagnation region extends further upstream. This would mean that the air flow over the surface within the forward stagnation no more has velocities of the order of the free stream velocities and even though turbulence may increase in this region, the ability of the flowfield to transport heat is throttled because of the reduced velocities in this region. At the tip of the horn, free stream velocities still exist, hence not much difference in the heat transfer coefficient is noted. This change in the heat transfer coefficient and flowfield with time changes the rate at which and quality, or surface structure of the ice forming. At time zero, the surface of the cylinder is clean and smooth. The heat transfer rate is maximum at the forward stagnation point. Water droplets that impinge on the surface do not freeze on contact, but flow along the surface downstream as they lose heat. The front surface of the cylinder is the only face that has water droplets impinging on its surface. Any water that may arise on the aft face is due to it flowing along the surface and around. If the distribution of water droplets within the flowfield is homogeneous, then the rate at which these droplets impinge on the upstream surface of the cylinder should be proportional to the elemental surface area component normal to the direction of the free stream, the flow given by $RCos\theta dy dz$. However, when inertia of the droplet and drag due to shear with the flowfield is considered, depending on the size of the droplet, the distribution or local collection efficiency of the

surface changes^{17,19,22}. The supercooled water droplets due to their inertial forces deviate from the curvature of the streamlines in the vicinity of the leading edge. The larger droplets deviate more from the streamlines having less curved trajectories. Coupled with this is the fact that the droplets do not freeze on contact but flow along the surface. Thus the rate of ice buildup at any location depends on the local heat transfer coefficient and the net rate at which water is transported into the region. The shift from the metastable thermodynamic state of supercooled water to the more stable state of ice is precipitated by a physical disturbance. Changes within the velocity field are sufficient conditions to initiate such shifts. As the ice accretion increases in size the stagnation region extends further upstream of the body, thus the supercooled water droplets experience velocity changes much ahead before collision with the body. Consequently the phase change process of water to ice begins before contact. Depending on the size of the water droplet, the ability of it to release heat to the ambient, the droplet will impact the surface fully or partially frozen. If partially frozen, the shell like ice ball will break up on impact, releasing its water contents which flows and freezes. The solid droplets will freeze on impact. All the above, the solid frozen droplets, droplet shell fragments and waves on the water surface constitute the surface roughness.

SAND GRAIN ROUGHNESS

It is customary in fundamental fluid mechanics research applications to introduce an equivalent sand grain roughness, k_s . By definition it is the size of uniform sand grains that produces the same wall shear stress as the actual roughness under the same flow conditions⁴². Schlichting⁴³ introduced this concept when he attempted to correlate his skin friction vs surface

roughness data, with the data previously obtained by Nikuradse⁴⁴ for rough pipes. The experiment⁴³ was set up such as to provide a region with a fully developed turbulent boundary layer in a rectangular channel, in which the measurements, for surfaces implanted with elements of differing shapes, sizes and interspaces, were taken. By using velocity profiles and pressure drop data, Schlichting⁴³ and later Coleman⁴⁵ were able to arrive at the equivalent sand grain roughness. First, the experiment was such as to ensure a uniform pressure drop in the fully developed region from which the average wall shear stress could be calculated. Second, the velocity profile was assumed to be two-dimensional and invariant in the streamwise direction within the fully developed region.

For a given value of k , Equation (11) describes the "log law" velocity profile for fully developed turbulent flow over a rough wall,

$$\frac{u}{v_*} = 5.75 \ln\left(\frac{y}{k}\right) + B \quad (11)$$

solving for constant B , by fitting Equation (11) to the experimental data, and then using,

$$5.75 \log\left(\frac{k_s}{k}\right) = 8.5 - B \quad (12)$$

an average value of k_s for the whole roughened surface can be determined. Thus it is possible to compare the scale k of an arbitrary roughness with that of a standard roughness k_s ^{43, 45, 46}.

Experiments were performed to measure the velocity and temperature over a 3-D grid in the forward stagnation region of the 15 minute glaze ice smooth and rough models, (see Fig (7,14)). The stagnation zone extends up to four diameters upstream. There is no significant change in the velocity profile

without or with the rough skin included. Temperature measurements using a hot wire in the forward stagnation zone indicate that the flow unsteadiness is responsible for temperature variations which extend into the zone for about an inch at the line of symmetry. Within one diameter upstream of the surface, the flow is decelerated to 30% of the free stream value(all velocities measured in this region are aggregates), the flow being irregular, unsteady, the turbulence intensity reaching up to 5% of the free stream velocity (viz. 60% of local velocity,— this includes contribution of unsteady flow). Unlike the experiments in fully developed internal flows^{43,44}, velocity boundary layers in external flows keep growing. On a given surface, the Reynold's number increases as the flow moves downstream, and the boundary layer which has zero thickness at the forward stagnation, thickens concurrently. The fact that the temperature variation extends about an inch at the line of symmetry may be due to the high local turbulence intensity and flow unsteadiness. No recirculating flows have been detected in this region using smoke. At the tip of the horn, where free stream velocities exist, the thermal boundary layer thickness reduces considerably. Past the horn (which acts as an abrupt step), and downstream, the flow encounters high pressure gradients, which induce separation of the velocity boundary layer. Numerical studies³², velocity flow measurements, and flow visualization using smoke, performed by the authors and others⁴⁷, clearly show these trends in flows over highly curved concave passages. Such flow conditions were also noted for the glaze ice without the rough skin. This would mean that the predominant flow characteristics in this region of the forward stagnation are determined primarily by the larger horn like protuberances of the glaze ice rather than the local surface constituting the skin.

Velocity profiles which were taken over a coarse grid do not show any similarity. Secondly, the surface is not of uniform sized roughness. Accordingly, if the analysis used by Coleman⁴⁵ was applied, one would arrive at equivalent sand grain roughnesses which vary with the location on the surface. Such an equivalent description of roughness holds no advantage over the Fourier description, as velocity profiles have to be obtained at each point in order to calculate the equivalent sand grain roughness at that location. Introduction of such roughness factors into complex numerical codes further exacerbate the solution of the problem if several sandgrain roughnesses have to be used. This suggests that the Fourier data be used to obtain surface characteristics needed to determine the flow, thus introducing simplifications to the geometry.

A surface is rough if the roughness elements are large enough to protrude above the laminar sublayer. Thus disturbances created by the flow around the obstruction will produce turbulent motion very near the wall. The flow over a rough surface must depend intimately upon the size, shape, and distribution of the roughness elements and upon the friction velocity v_* . To specify the size of a roughness pattern, a typical dimension, 'k', is used⁴⁸. This dimension k is identical to double the amplitude of the sinusoidal function (equivalent to the total peak to valley distance), given by the Fourier coefficients. The width and spacing λ are given by the inverse of the frequency of the function, see Tables (4,5).

Schlichting⁴³ from his experiments observed that for elements of a given height there exists a configuration which produces the maximum drag, the spacing in this being far more than that for a densely packed surface^{49,50}.

Owing to the close proximity of the elements in a densely packed surface, the growth of the disturbances shed by neighbouring elements is partially inhibited, thus indirectly having a shielding effect on each other. With this in mind let us consider the results of the Fourier analysis on both the whole 15 minute glaze ice and its superficial rough skin. From Table (4) we see large roughness elements of amplitude $0.78 < (A, B) < .38$ inch and large wavelength $1 < \lambda_0 < 3.14$ radian, which corresponds to the horns of the glaze ice, between which the far smaller elements of the rough skin (details in Table (5)) are packed. The form drag is insensitive to the low values of surface roughness of the skin within the concave region of the upstream section of the glaze ice (see Koh⁴⁷ and Nikitin⁵¹), and is primarily caused by the point of separation that is determined by the edges of horn of the glaze ice. Now, if we calculated a mean roughness height on the whole surface grid, it would be considerably reduced in magnitude compared to that of the dominant horn of the glaze ice. From this we can conclude that the effective roughness, k , should be weighted in favour of the larger elements present in it.

The fluid being air and having a Prandtl number of 0.7 would mean that the thermal and velocity boundary layers would develop similarly. This would mean that if the introduction of the rough skin on the smooth glaze ice were to significantly change the velocity boundary layer, then a like effect should be seen in the thermal boundary layer. Hence, determination of the local heat transfer coefficient without (given in Chapter 2) and with the rough skin will indicate the effect of this superficial skin.

HEAT TRANSFER CHARACTERISTICS

Having already obtained satisfactory heat transfer data on the surface of simulated smooth glaze ice profiles (see Chapter 2), the next step was to determine the heat transfer coefficient with the rough skin. The measurement techniques and apparatus are described in detail in the previous chapter. The process of preparing a rough skin is given in FABRICATION.

Skin Correction

The thin skin, which makes up the rough projections on the surface, Fig (11), is cast on top of the thermocouples. The finite thermal conductivity of this skin material requires that the experimental procedure incorporate a temperature correction such as to arrive at the required surface temperature. From Fourier's Law of heat conduction we have,

$$Q = KA(T_m - T_s)/dx$$

or,

$$T_s = T_m - Qdx/kA$$

where,

T_s ----- actual surface temperature °C

T_m ----- measured temperature °C

Q ----- local heat flux W/m.K

dx ----- skin thickness m

K ----- Thermal conductivity W/m.K

A ----- normal area m^2

The temperature of the rough skin undersurface (T_m) is measured using thermocouples. On site temperature corrections are made until the required actual surface temperature(T_s) is obtained.

The skin thickness, dx , varies anywhere from 1mm to 5mm on the undulating surface. This introduces, for a uniform heat flux over each heater element, an uncertainty in the actual surface temperature, resulting in a corresponding uncertainty in the Nusselt number. Secondly, in calculating the heat transfer coefficient given the heat flux the surface area is required. Most published results use the smooth surface (plan area) whose normal is perpendicular to the direction of flow. Having obtained the coordinates of the surface we also obtained the true rough surface area using surface integration. Depending on the location these true areas are upto 1.9 times the smooth areas.

The transfer of heat from the surface occurs in the first place by purely molecular diffusion through a film of air. Above this laminar sublayer there is a transitional layer in which turbulent exchange increases rapidly and becomes the over-riding process at the base of the region of fully developed turbulent flow. This implies that the molecular conduction process is the major source of resistance^{51,52} to the transfer of heat within the boundary layer. That much of the resistance to heat transfer occurs in the layers close to the surface is exhibited by the fact that typically more than half of the difference in temperature between the surface and the ambient takes place over the laminar sublayer⁵³.

Typical results of Nusselt numbers obtained for both the smooth and rough 15 minute glaze ice models are provided. Fig (15) is a plot of the local Nusselt number calculated using the plan area. The 'I' symbols indicate the range of uncertainty due to temperature. Within the forward stagnation zone (up to $\psi=38^\circ$), an increase of 53% at the centerline and up to 115% at the tip

of the horn in the heat transfer is realized. Downstream this increase lies anywhere between 40% to 120%. Fig (16), provides a comparison of the Nusselt number of the same data, the difference being that the actual rough area is used in the calculations. Here we see that the Nusselt number actually decreases in the forward stagnation zone showing an increase only at the tip of the horn of about 50% and further downstream between 20% to 90%.

The total heat transfer rate over the whole rough surface shows an increase of up to 40%, 75% of which is due to the downstream surface from the horn. The region of importance is the location where the maximum heat flux occurs. This occurs at the tip of the horn, where an 80% increase in the Nusselt number is observed. The surface downstream of this section supports higher Nusselt numbers, but, the incidence of water flow in this region is low⁴ and hence, comparatively of less significance. All the above percentages are relative to the smooth glaze ice data. The above analysis suggests that within the forward stagnation zone of the rough model the augmentation in heat transfer is partially due to the increase in surface area. Icing studies performed in the past⁴ indicate that icing is predominant on the horn and tops of the large roughness elements. This again leads us to conclude that the large amplitude, low frequency elements of roughness, such as the horn, determine the flow characteristics.

Two other authors', namely, Van Fossen³¹ and Arimilli²⁹ have also performed experiments on similar glaze ice models. Van Fossen³¹ used sand grains, while, Arimilli²⁹ employed tripping wire loops to simulate the effect of roughness on the boundary layer. The authors' data are compared in Fig (15) with the above published results. The data compare well in trend. Ari-

milli's²⁹ data, on the average over the whole surface, show a 4% to 28% decrease in the Nusselt number when compared to those of the authors'. When compared to their²⁹ own smooth glaze data the increase is of the order of 44%. Van Fossen's³¹ data on the other hand, are higher than the authors on the average by 21% to 58%. When their³¹ rough model data is compared to that of their smooth model an increase on the average of 28% is seen. At the tip of the horn theirs³¹ show the highest values for Nusselt number for both smooth and rough models, being 120% higher than the authors' in this region.

CHAPTER 4

Very little work has been done in determining the local heat transfer coefficients for airfoil surfaces. The literature is flooded with lift and drag data^{4,7,21,54} but few have looked into the thermal aspects. This most probably is because problems like ice accretion have only become of strategic importance lately and renewed interest is now coming to light with missions of missiles and aircraft which have to be flown in such conditions. Having already performed detailed local heat transfer measurements on ice accretions on a cylinder, the next step was to perform similar experiments on glaze ice accretions on airfoils.

A number of experiments in ice accretion have already been performed^{4,19,21} on the NACA 0012 airfoil to determine its aerodynamic characteristics. It was decided to select this profile which is commonly used on helicopters because of its appropriateness to the problem since such aircraft are most susceptible to icing as they are required to fly at lower altitudes. Secondly, the determination of the local heat transfer coefficient would complete the data bank available for both the fluid and thermal fields of this airfoil. Two models were selected for the present study, namely, a smooth NACA 0012 airfoil and a 5 minute glaze ice accretion on the same airfoil, the flow conditions for which are detailed in reference⁴.

FABRICATION

Since ice accretion is predominantly a leading edge phenomenon, heat transfer measurements were performed only on a section of the leading edge. The airfoil is constructed of Steel-Aluminum laminate. This being a good conductor of heat requires that a section be cut off and replaced with an insulating

piece (Balsa wood) of the same profile. The heaters and thermocouples were mounted on this wooden section consistent with fabrication methods described earlier in Chapter 2. The Chord for NACA 0012 is $C=536$ mm. The 'l/C' from stagnation, is the dimensionless length from the point of stagnation at $\alpha=0^\circ$ angle of attack. The wing spanned the full height of the test section and was mounted such that its angle of attack could be varied through a wide range. The smooth model surface is heated using 20 independent Minco thermo-foil heaters 5.9 mm x 175 mm x 0.3 mm, glued without spacing onto the surface of the wooden body insert of the model. The heaters cover 5% of the chord on one face of the leading edge and 20% of the chord on the other face of the leading edge. In order to obtain data at various angles of attack for both the pressure and suction surfaces, the experiments had to be performed twice for the same Reynold's number with the heated section first in the suction region and then aligned so as to be in the pressure region of the flow.

RESULTS

Fig (17) is a plot of the Nusselt number (based on chord) variation with l/C at $\alpha=0$ to 8° for the airfoil without ice accretion. When compared to $\alpha=0^\circ$, there is an increase in the average heat transfer over the forward 18% of the chord surface region by up to 20% for $\alpha=2^\circ$. $\alpha=4^\circ$ also shows an increase in the overall average heat flux over 18% of the chord by up to 14%. At $\alpha=6^\circ$, there is a 25% increase over 18% of the chord and for $\alpha=8^\circ$ a 27% increase over the same region is noted. Fig (18) is a plot of the Nusselt number (based on l) variation with l/C at $\alpha=0^\circ$ to 8° . Since l increases as the flow moves away from the stagnation, the Nusselt number shows an increasing trend on both the suction and pressure surfaces, the higher values being registered as is expected on the suction face. From both Fig (17,18), as the angle α

increases, the Nusselt number on the suction surface increases, that on the pressure surface decreases at any location, a far greater increase being observed on the suction surface. At $\alpha=2$, 4 , 6 and 8° the average relative increase of the Nusselt number on the suction surface with respect to the pressure surface is 21 , 36 , 58 and 72% respectively, an approximately linear increase with angle of attack. This implies that most of the increase in the Nusselt number is realized on the suction surface and if ice accretion were to occur, one should expect a larger horn on this side of the stagnation. However, the pressure surface is predominantly facing the flow, and hence collects most of the accretion. The above experiments were performed in the Reynold's number range of $760,000$ to $2,000,000$ based on chord. Given any angle of attack, experimental data in the form of Nu/\sqrt{Re} correlate very well within the tested range of Reynolds numbers. Within the tip or stagnation region of the airfoil, (see Fig (17,18)), the Nusselt number is almost independent of the angle of attack, more so on the pressure surface. The same is true in the stagnation region of a cylinder, and if the nose of the airfoil is approximated to be a cylinder, then this association is clearly noted, (see Fig (3)).

As already determined from studies performed on large glaze ice accretions, the geometrical quality of a surface that determines the flow field are the larger elements in the forward stagnation region, ie., the large ice accretion shape forming on the nose of the airfoil must be considered as the primary roughness. Thus a smoothed profile of a 5 minute glaze ice was generated from the rough surface⁵⁴. This smooth profile Fig (19), makes experimental fabrication and measurements more feasible. Fig (19) shows the forward section of the NACA 0012 airfoil with the 5 minute smooth glaze ice

shape attached. Coordinates of the above section along with thermocouple locations are provided in Table (6). Note that this experiment was performed at $\alpha=4^\circ$. The surface of the 5 minute glaze ice model was heated using 13 independent Minco heaters 5.9 mm x 140 mm x 0.3 mm. The heaters cover the total projecting surface of the 5 minute ice shape in the forward stagnation region of the airfoil. Fig (20a) illustrates the Nusselt number variation along the surface of this model with time at the same angle of attack for $t=0$ and 5 minutes of icing. When Nusselt number is defined using C, it is observed that a predominant peak occurs at $1/C = -3.2\%$ of the chord along the suction surface and then levels off for the rest of the surface. From Fig (19) we note this region of high heat transfer corresponds to thermocouple number 2 which is located on the tip of the budding horn. The Nusselt number has decreased by almost 25% of its original value at $t=0$, over most of the remaining glaze ice surface. Fig (20b) indicates that when the Nusselt number is based on 1, no significant difference is noted in the heat transfer characteristics with or without a glaze ice accretion. This would mean that heat transfer data obtained for the smooth airfoil can be used for the prediction of ice accumulation at later periods in time. Experiments were performed in the Reynolds number range of 960,000 to 1,800,000. The Nusselt number again appears to be a function of the square root of the Reynolds number. Fig (21) is a contour plot of time averaged velocities around this model. Note the region of separation on the suction side of the model adjacent to the horn.

CONCLUSIONS

The technique used by the authors to measure the heat transfer coefficient gave good, reproducible results. The smooth ice shape models were prepared

meticulously, with precautions taken to conform to the initial profile as closely as possible. Heat transfer results agree well with those of Van Fossen³¹. Arimilli's²⁹ data show similar trends but are lower in magnitude. Both Van Fossen³¹ and the authors' models were almost identical in size and shape. Arimilli²⁹ used a transient method to measure the heat transfer coefficient and his models were geometrically similar but mounted on a cylinder 63.5 mm in diameter. A better correlation exists between Nusselt number and angle from stagnation than between the Nusselt number and 1/D.

The heat transfer coefficient decreases with growth of the ice. When the Nusselt number is based on the maximum width of the profile subtended by the flow, which includes the ice growth, the data from the different ice profiles tend to coalesce.

Fourier coefficients were obtained for both the whole glaze ice profile and its hypothetical superficial rough skin. This skin can be numerically transplanted on other glaze ice models to calculate local characteristics if necessary. From the Fourier analysis, fluid flow, and heat transfer measurements, we note that the key determining features of the 15 minute glaze ice geometry are the large wavelength, high amplitude components. In other words the whole ice accretion on the cylinder should be considered as the primary roughness element. The superficial, smaller, higher frequency components do augment the heat transfer by a factor which is approximately proportional to the increase in area subtended by these secondary roughness elements. No single sand grain roughness can be assigned to the profile.

When results of the actual rough model are compared with those of the smooth glaze ice it is observed that,

(a) a maximum increase of 115% in heat transfer rate occurs at the tip of the horn.

(b) there is an average increase in the heat transfer over the whole surface of 40%.

Local Nusselt numbers were also obtained for a NACA 0012 airfoil at various angles of attack. The suction surfaces show the higher values with increasing α . The forward stagnation region shows similar results to that of a cylinder. When data from a 5 minute glaze ice are compared to that of the smooth airfoil, no significant difference is noticed in the local Nusselt number when it is based on 1. This would mean that smooth airfoil data can be used in the prediction of ice accretion at later stages in time τ .

ACKNOWLEDGEMENTS

The authors would like to acknowledge the financial support given by the Air Force Systems Command and the Computational Aerodynamics Group at the Flight Dynamics Laboratory, Wright Patterson Air Force Base, Dayton, Ohio. They would like to thank Drs. Wilbur Hankey, Vladimiro Calarese and Joe Shang for their several suggestions and helpful discussions. Help rendered by Dr. R.C. Birkebak at the initial stage is also acknowledged.

The authors would also like to thank Mr. Lin Zou for his painstaking measurements of the velocity fields around the 15 minute rough glaze ice on a cylinder and the 5 minute glaze ice on a NACA 0012 airfoil.

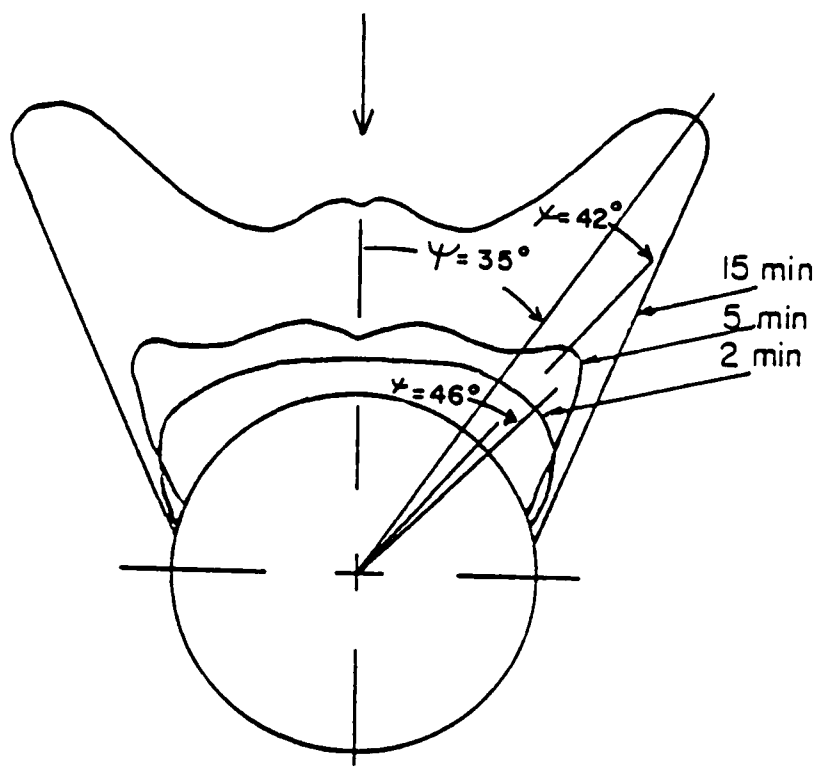


FIG. (1) 2, 5, 15 Glaze Ice Profiles

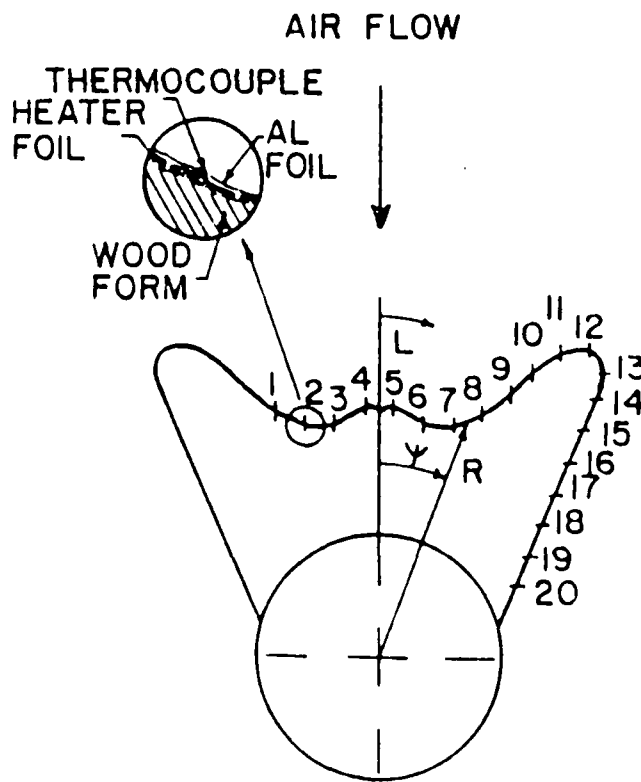


FIG. (2) Heater and Thermocouple Layout on Ice Model

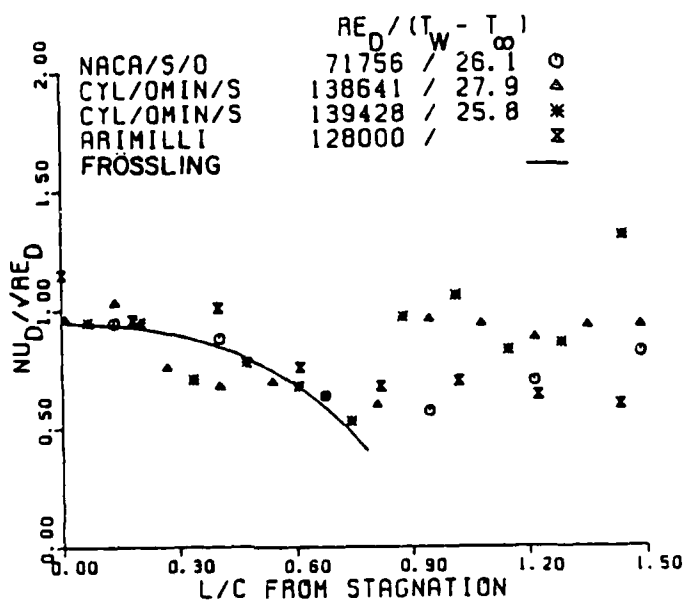


FIG. (3) Local Nusselt Number on Cylinder and Airfoil

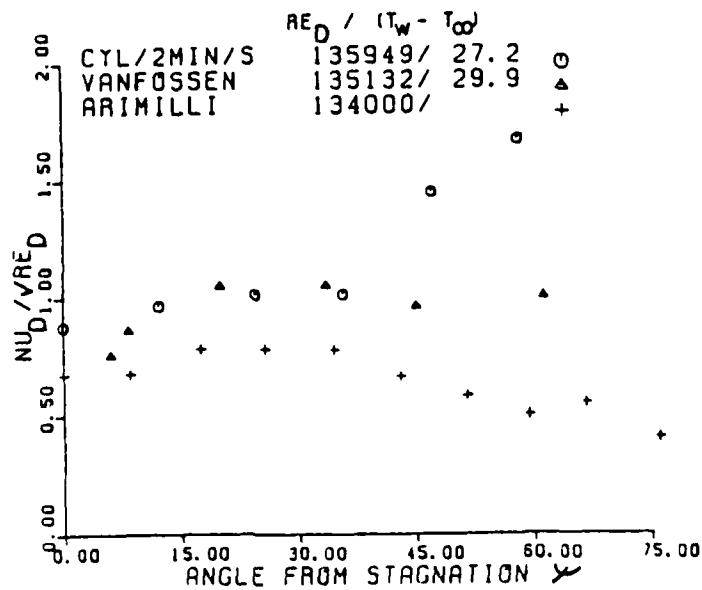


FIG. (4) Local Nusselt Number on 2 Minute Model

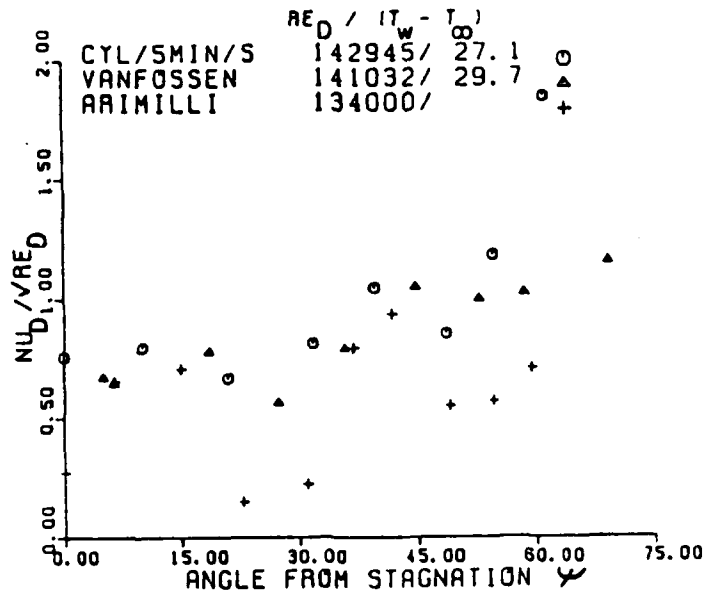


FIG. (5) Local Nusselt Number on 5 Minute Model

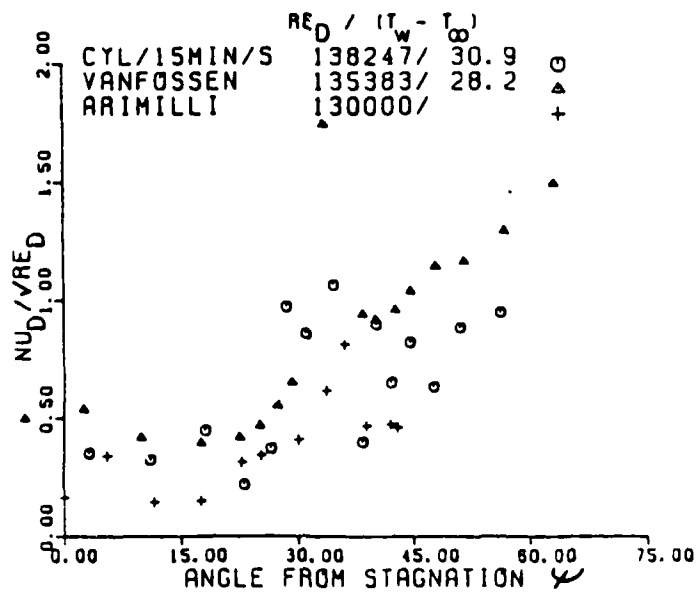


FIG. (6) Local Nusselt Number on 15 Minute Model

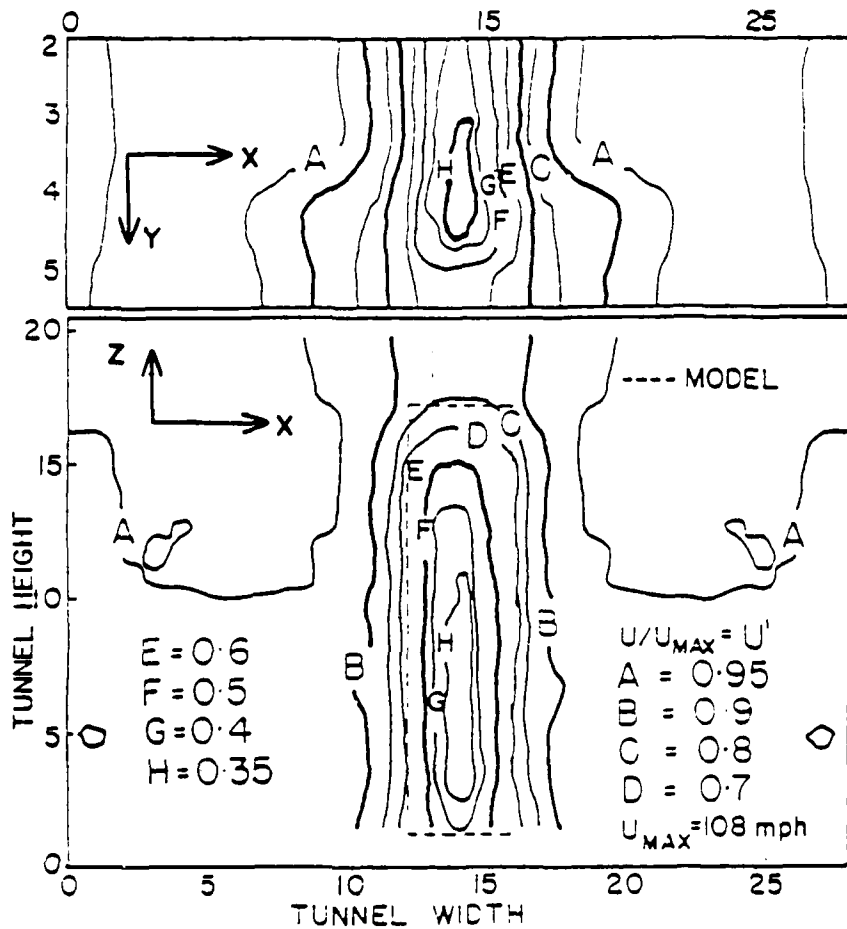


FIG. (7) Velocity Field Upstream of 15 Minute Smooth Model

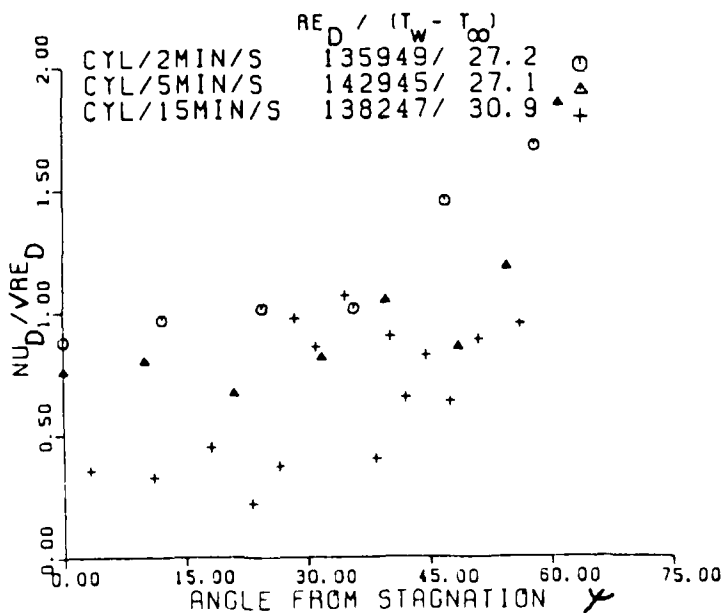


FIG. (8) Comparison of Local Nusselt Number with Ice Growth

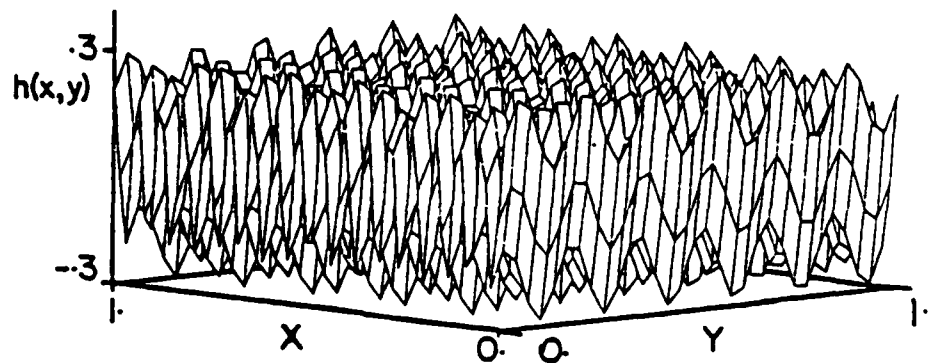


FIG. (9a) Surface Profile $h(x,y)$

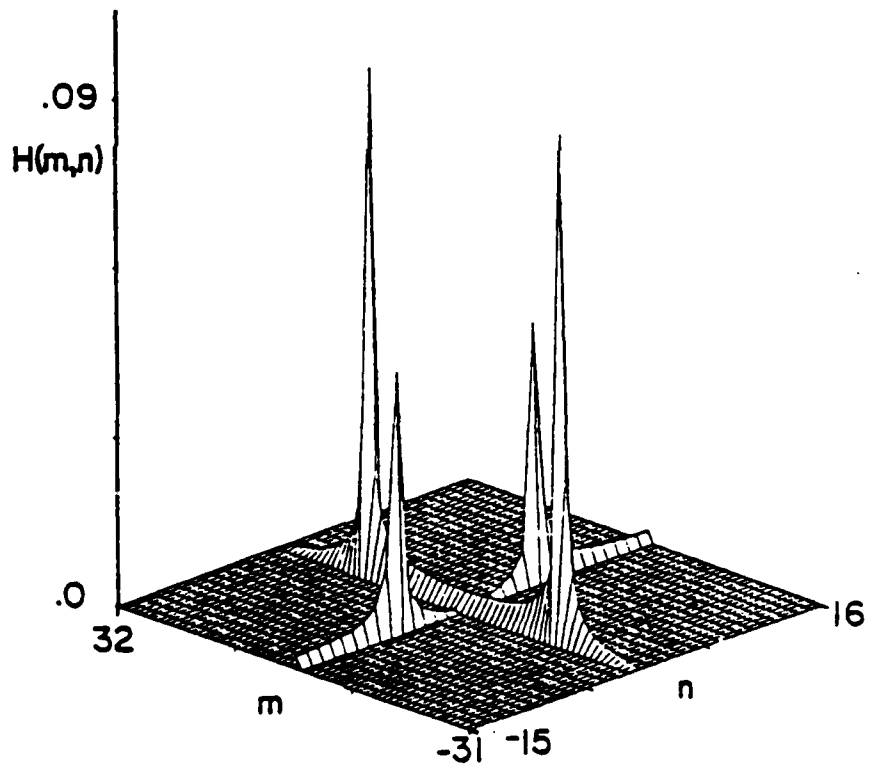


FIG. (9b) 2-D FFT $H(m,n)$

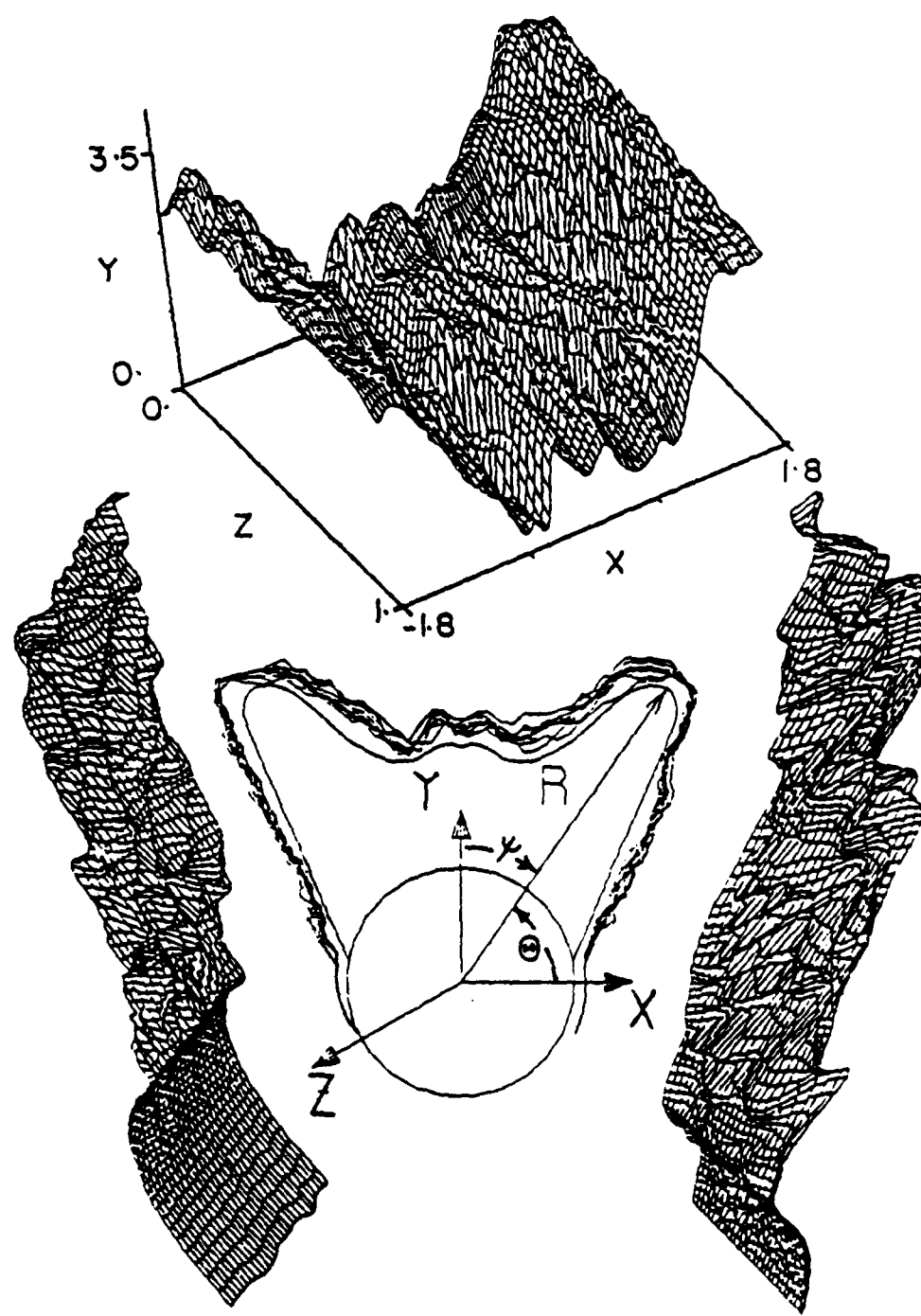


FIG. (10) True Surface Profiles of 15 Min. Model

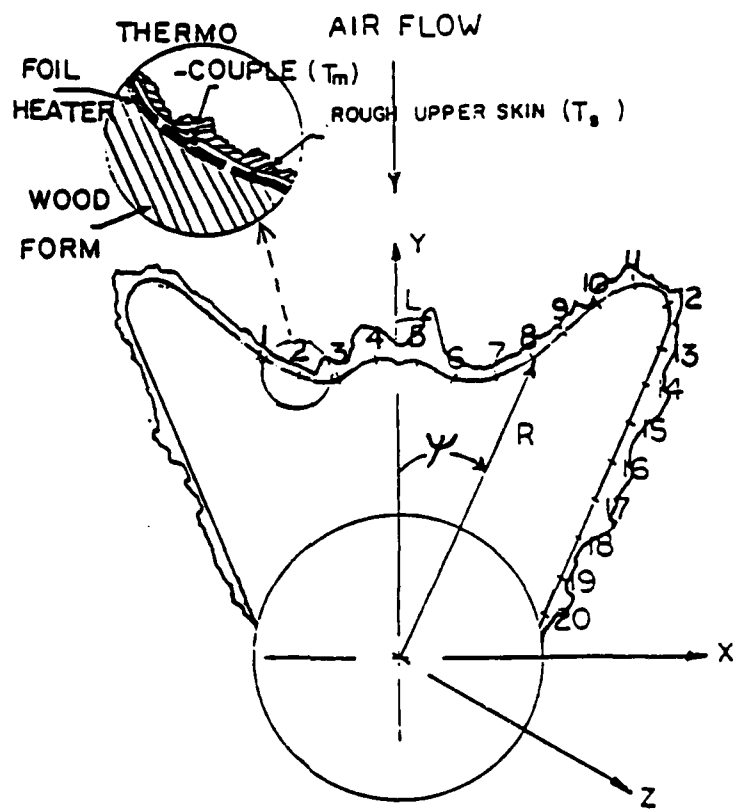


FIG. (11) Heater and Thermocouple Layout on Rough Ice Model

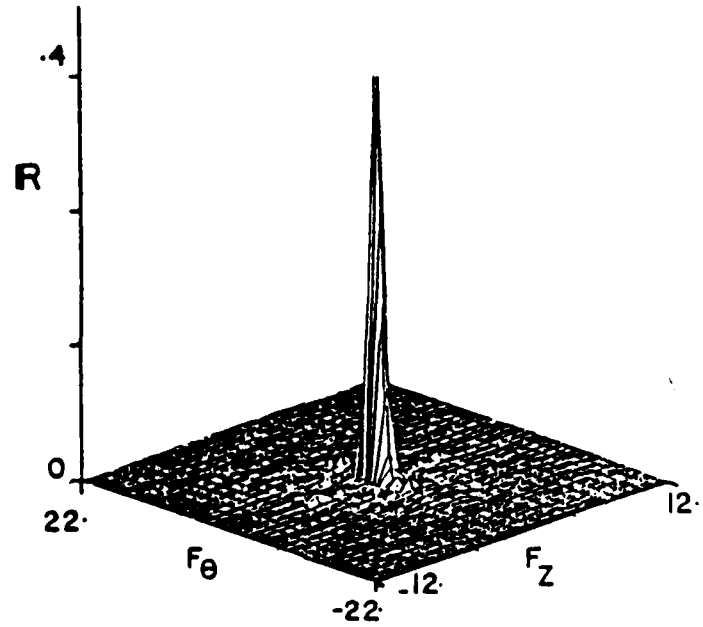


FIG. (12) 2-D FFT $R(F_\theta, F_z)$

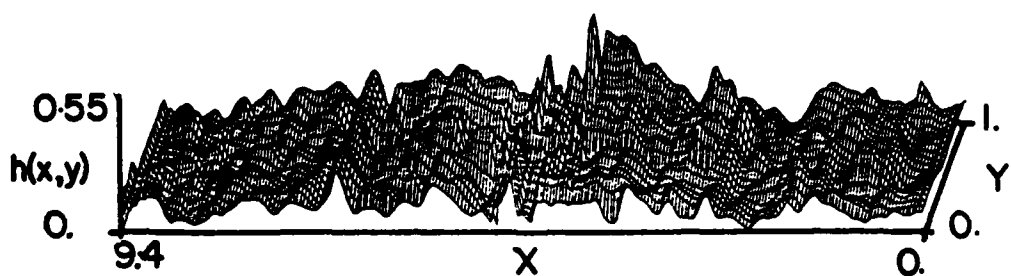


FIG. (13a) 15 Minute Rough Skin Surface Profile

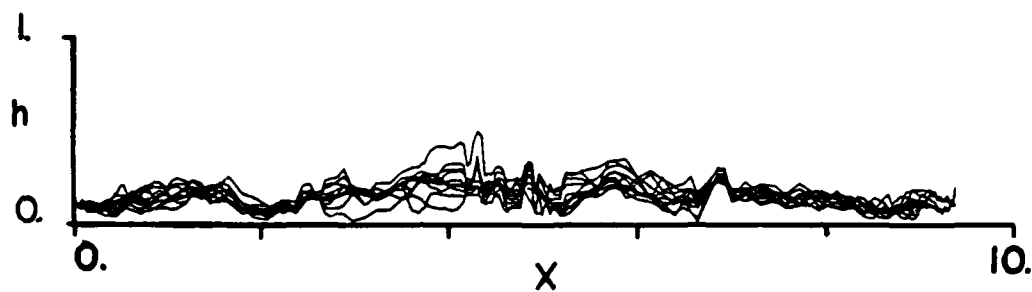


FIG. (13b) 15 Minute Rough Skin Profiles

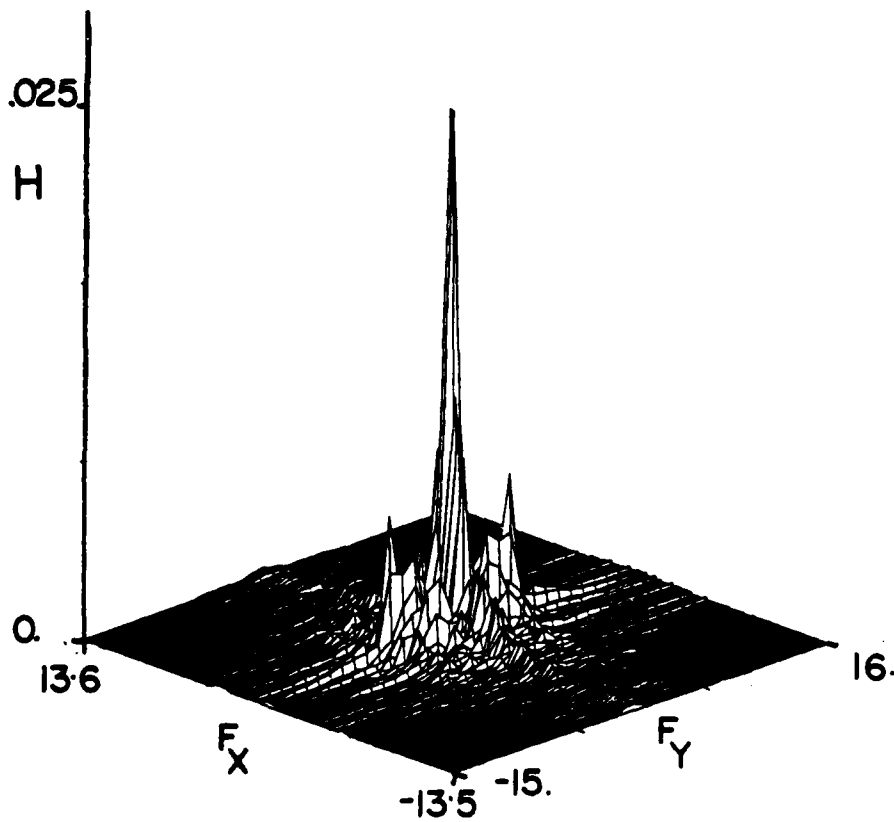


FIG. (13c) 2-D FFT $H(F_x, F_y)$

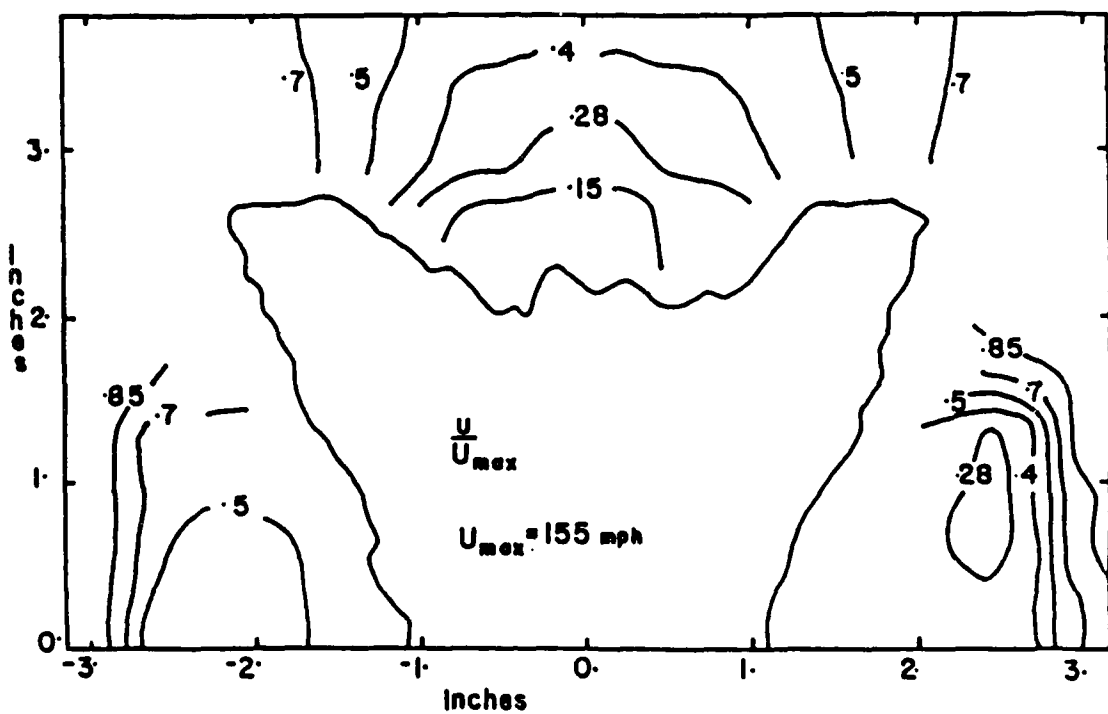


FIG. (14) Velocity Field Around 15 Min. Rough Model

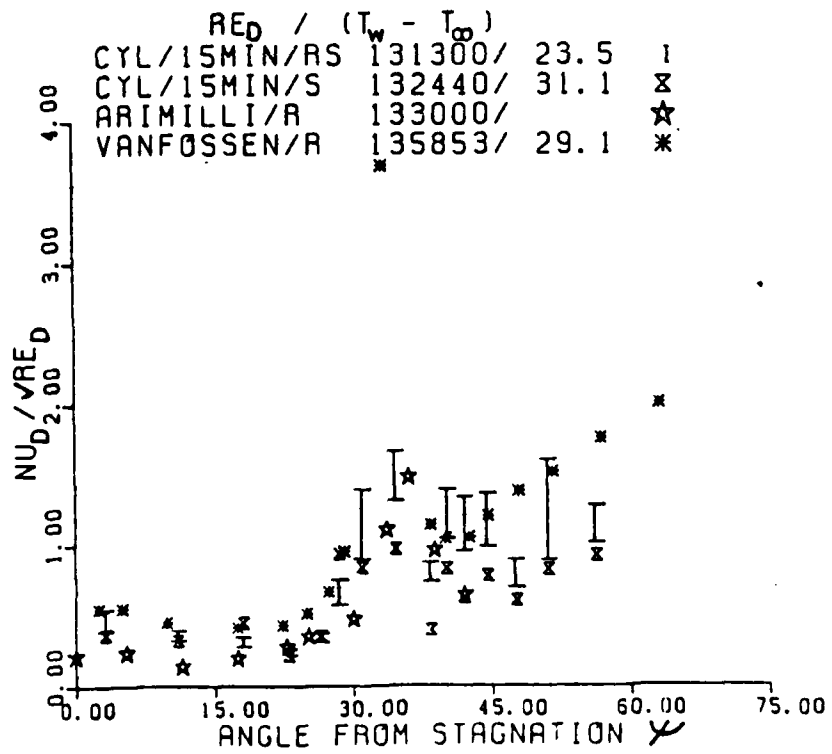


FIG. (15) Local Nusselt Number Using Plan Area

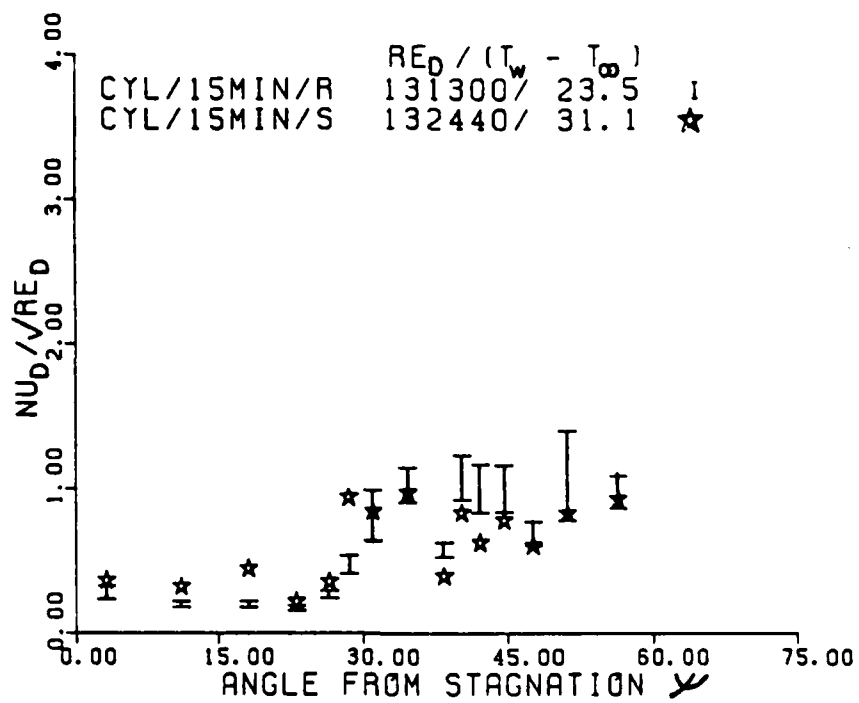


FIG. (16) Local Nusselt Number Using True Area

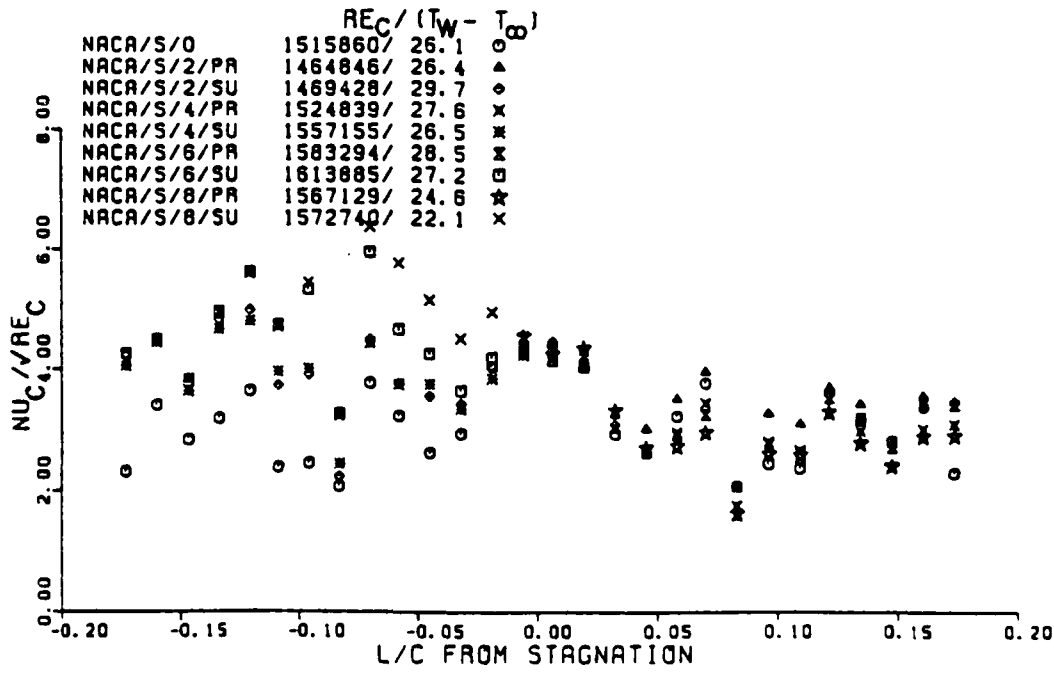


FIG. (17) Local Nusselt Number (C) on 0 Min. NACA 0012

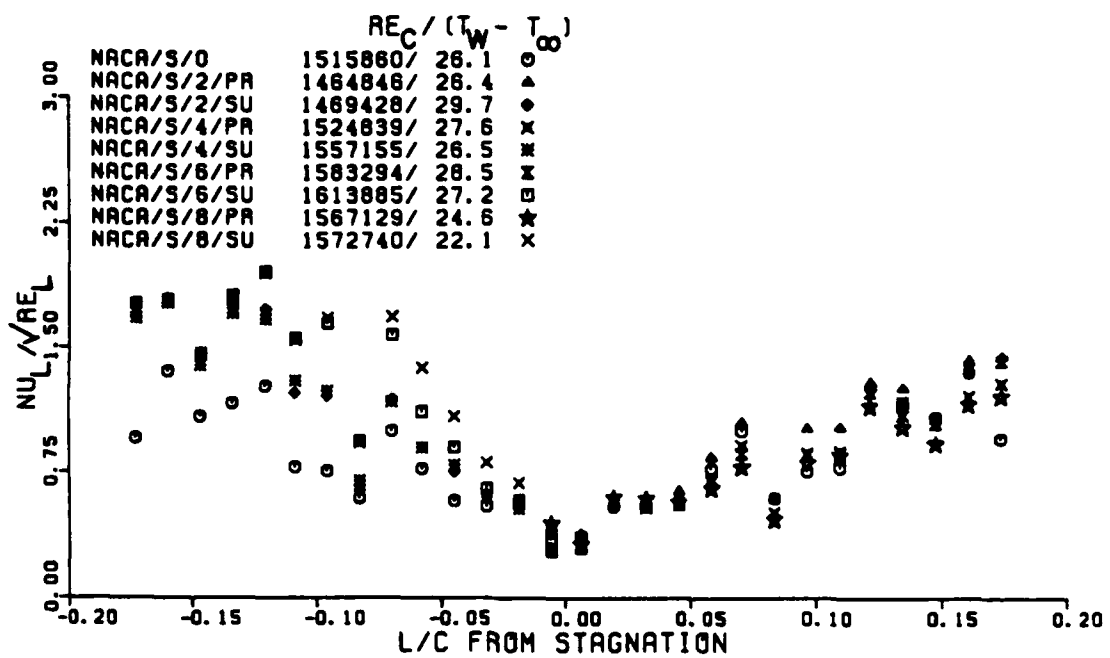


FIG. (18) Local Nusselt Number(l) on 0 Min. NACA 0012

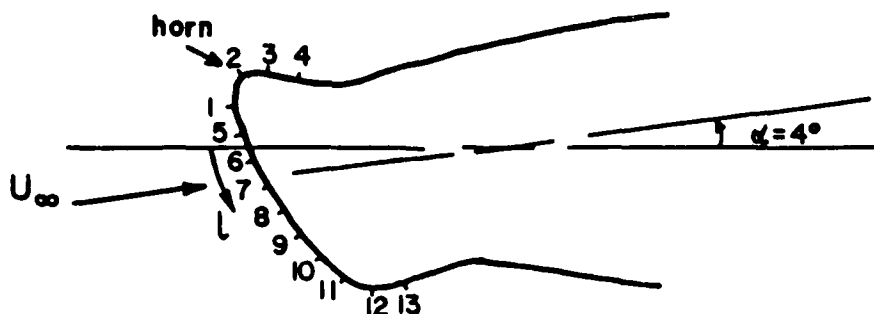


FIG. (19) 5 Minute Glaze Ice Profile on NACA 0012

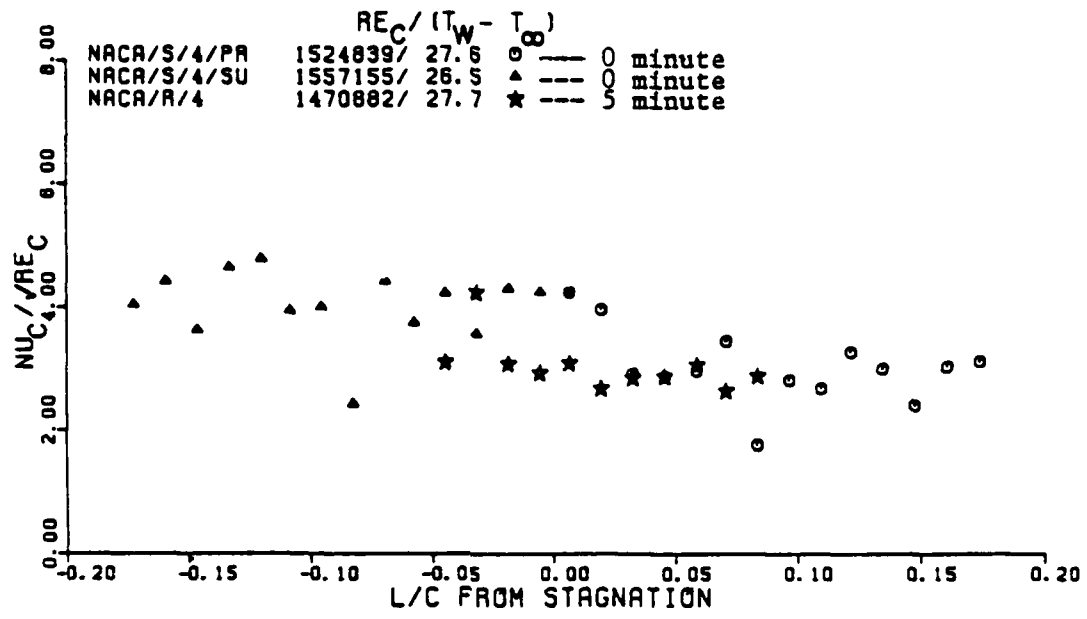


FIG. (20a) Local Nusselt Number(C) on 0 and 5 Min. NACA 0012

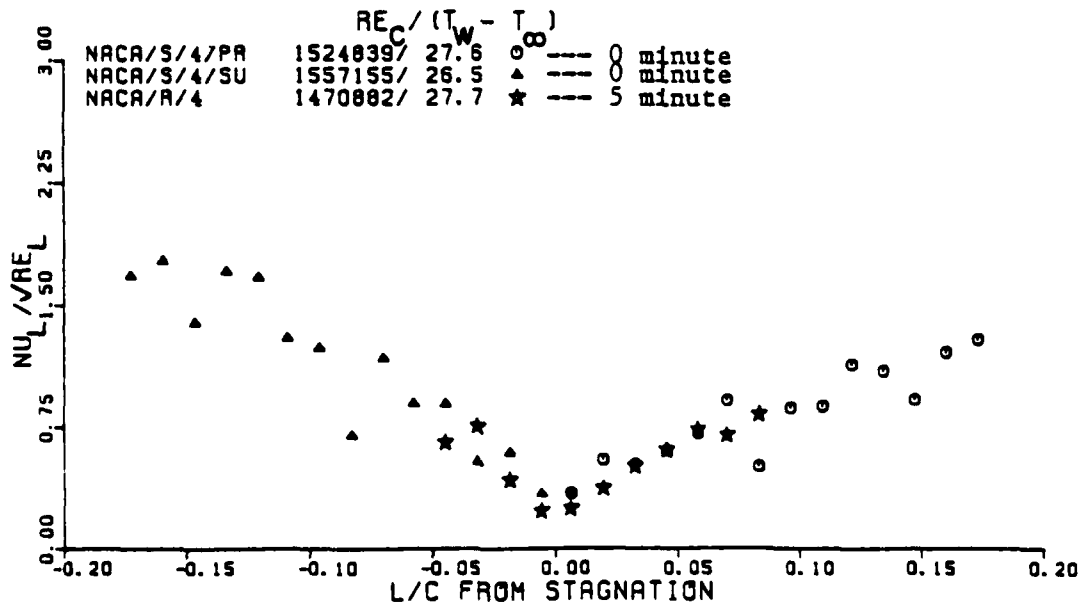


FIG. (20b) Local Nusselt Number(l) on 0 and 5 Min. NACA 0012

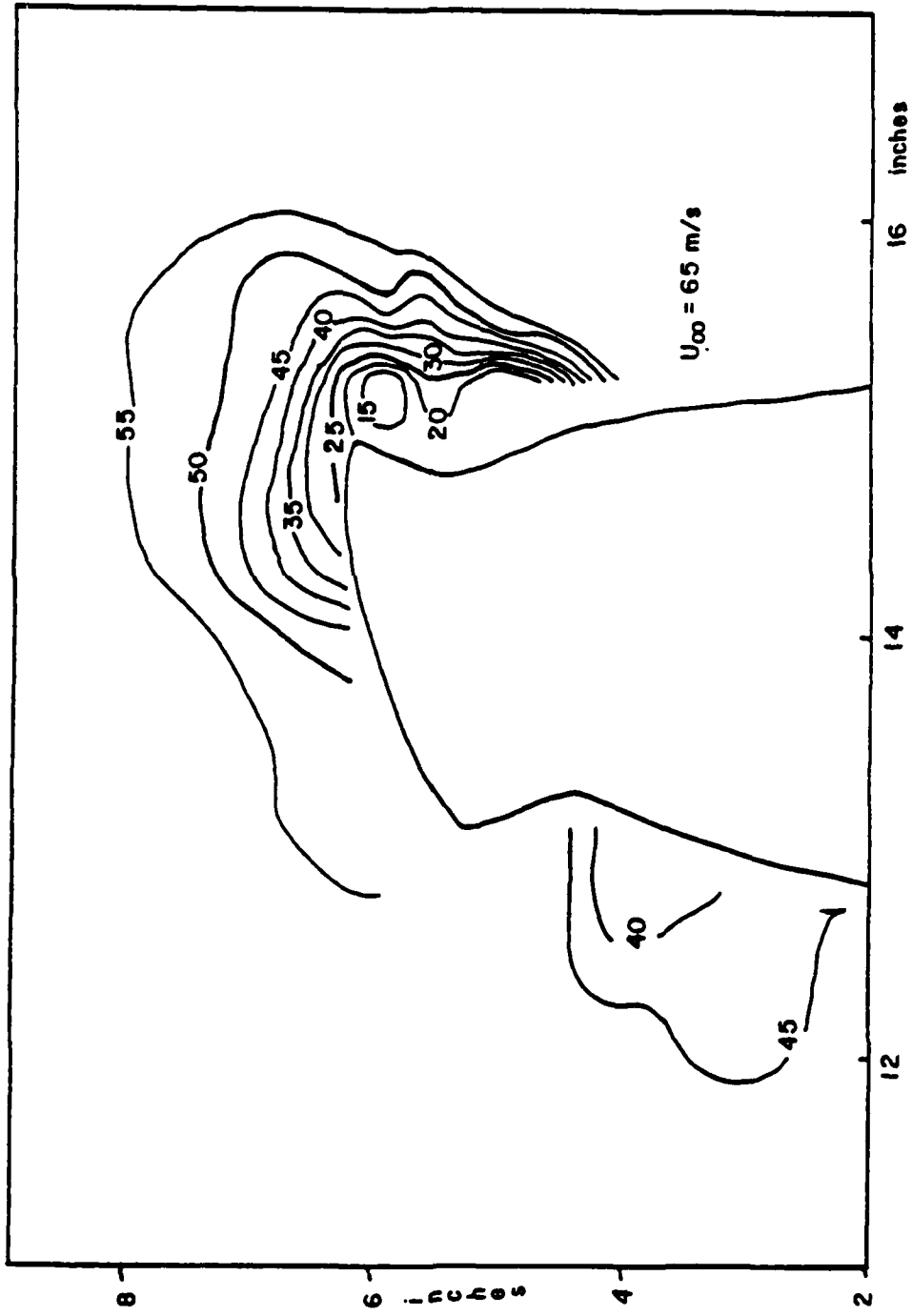


FIG. (21) Velocity Field Around 5 Min. NACA 0012

TABLE (1)

Coordinates of 2 minute glaze ice on cylinder							
Diameter of cylinder D=2. inches							
$R = 2 \cdot r/D$ r ----radius							
ψ ----angle from forward stagnation in degrees							
ψ	R	ψ	R	ψ	R	ψ	R
0	1.185	20	1.24	40	1.32	60	1.24
1	1.186	21	1.24	41	1.323	61	1.225
2	1.187	22	1.245	42	1.325	62	1.2
3	1.187	23	1.245	43	1.325	63	1.19
4	1.187	24	1.25	44	1.33	64	1.185
5	1.19	25	1.255	45	1.33	65	1.165
6	1.193	26	1.26	46	1.335	66	1.155
7	1.195	27	1.26	47	1.335	67	1.14
8	1.195	28	1.265	48	1.33	68	1.125
9	1.2	29	1.27	49	1.33	69	1.11
10	1.205	30	1.28	50	1.328	70	1.09
11	1.205	31	1.285	51	1.328	71	1.085
12	1.205	32	1.29	52	1.32	72	1.065
13	1.21	33	1.295	53	1.315	73	1.05
14	1.21	34	1.295	54	1.31	74	1.02
15	1.213	35	1.3	55	1.3	75	1.
16	1.22	36	1.305	56	1.29	76	1.
17	1.23	37	1.305	57	1.28	77	1.
18	1.235	38	1.31	58	1.27	78	1.
19	1.235	39	1.32	59	1.255	79	1.
Heater and thermocouple location							
#----Heater number							
1----Distance from forward stagnation along surface							
#	ψ	1/D	#	ψ	1/D		
1	0.	0.	7	-12.2	-0.135		
2	12.2	0.135	8	-24.5	-0.27		
3	24.5	0.27	9	-35.7	-0.405		
4	35.7	0.405	10	-47.	-0.54		
5	47.	0.54	11	-58.	-0.675		
6	58.	0.675					

TABLE (2)

Coordinates of 5 minute glaze ice on cylinder							
Diameter of cylinder D=2. inches							
$R = 2 \cdot r/D$ r ----radius							
ψ -----angle from forward stagnation in degrees							
ψ	R	ψ	R	ψ	R	ψ	R
0	1.315	18	1.45	36	1.555	54	1.405
1	1.32	19	1.45	37	1.57	55	1.375
2	1.335	20	1.45	38	1.595	56	1.33
3	1.34	21	1.445	39	1.645	57	1.305
4	1.36	22	1.445	40	1.675	58	1.27
5	1.37	23	1.44	41	1.695	59	1.235
6	1.375	24	1.445	42	1.705	60	1.205
7	1.385	25	1.44	43	1.705	61	1.18
8	1.4	26	1.44	44	1.7	62	1.155
9	1.415	27	1.445	45	1.695	63	1.14
10	1.425	28	1.445	46	1.685	64	1.115
11	1.43	29	1.445	47	1.655	65	1.08
12	1.44	30	1.46	48	1.63	66	1.06
13	1.445	31	1.465	49	1.6	67	1.035
14	1.445	32	1.475	50	1.555	68	1.
15	1.45	33	1.485	51	1.515	69	1.
16	1.45	34	1.495	52	1.47		
17	1.45	35	1.52	53	1.435		

Heater and thermocouple location					
#-----Heater number					
1-----Distance from forward stagnation along surface					
#	ψ	1/D	#	ψ	1/D
1	0.	0.	9	-10.	-0.135
2	10.	0.135	10	-21.	-0.27
3	21.	0.27	11	-31.7	-0.405
4	31.7	0.405	12	-39.5	-0.54
5	39.5	0.54	13	-48.5	-0.675
6	48.5	0.675	14	-54.5	-0.81
7	54.5	0.81	15	-61.	-0.945
8	61.	0.945			

TABLE (3)

Coordinates of 15 minute glaze ice on cylinder							
Diameter of cylinder D=2. inches							
$R = 2 \cdot r/D$							
ψ -----angle from forward stagnation in degrees							
ψ	R	ψ	R	ψ	R	ψ	R
0	2.06	20	2.1	40	2.88	60	1.35
1	2.07	21	2.13	41	2.73	61	1.32
2	2.08	22	2.18	42	2.58	62	1.3
3	2.09	23	2.23	43	2.47	63	1.27
4	2.08	24	2.28	44	2.34	64	1.25
5	2.07	25	2.34	45	2.25	65	1.22
6	2.06	26	2.44	46	2.15	66	1.2
7	2.05	27	2.56	47	2.07	67	1.18
8	2.03	28	2.68	48	1.98	68	1.15
9	2.02	29	2.8	49	1.92	69	1.14
10	2.	30	2.92	50	1.83	70	1.12
11	1.99	31	3.	51	1.78	71	1.1
12	1.98	32	3.05	52	1.71	72	1.08
13	1.99	33	3.1	53	1.65	73	1.07
14	1.99	34	3.12	54	1.62	74	1.05
15	2.	35	3.14	55	1.58	75	1.03
16	2.01	36	3.14	56	1.5	76	1.02
17	2.02	37	3.11	57	1.45	77	1.01
18	2.03	38	3.07	58	1.41	78	1.
19	2.06	39	3.01	59	1.39	79	1.
Heater and thermocouple location							
#----Heater number							
1----Distance from forward stagnation along surface							
#	ψ	1/D	#	ψ	1/D		
1	3.2	0.067	11	42.	1.417		
2	11.	0.202	12	44.5	1.552		
3	18.1	0.337	13	47.5	1.687		
4	23.1	0.472	14	51.	1.822		
5	26.5	0.607	15	56.2	1.957		
6	28.5	0.742	16	62.5	2.092		
7	31.	0.877	17	-23.1	-0.472		
8	34.6	1.012	18	-18.1	-0.337		
9	38.3	1.147	19	-11.	-0.202		
10	40.1	1.282	20	- 3.2	-0.067		

TABLE (4)

$A_0 = 2.09$ All Dimensions A, B, C, D in inches Wavelength λ in radians									
FFT IN Θ DIRECTION M=1,33									
λ_Θ	A	B	λ_Θ	A	B	λ_Θ	A	B	
3.14	-0.776	0.010	1.57	-0.544	0.020	1.05	0.338	-0.006	
0.79	0.098	-0.032	0.63	-0.188	-0.006	0.52	0.060	0.010	
0.45	0.028	0.026	0.39	-0.004	-0.010	0.35	-0.010	-0.018	
0.31	0.010	0.020	0.29	0.014	-0.010	0.26	-0.016	-0.002	
0.24	0.000	-0.006	0.22	0.006	0.002	0.21	0.014	0.006	
0.2	-0.032	-0.002	0.18	0.010	-0.002	0.17	0.008	0.004	
0.17	-0.002	0.000	0.16	-0.008	-0.002	0.15	0.010	0.002	
0.13	-0.006	-0.004	0.13	0.004	-0.006	0.12	0.004	0.004	
0.12	-0.004	0.004	0.11	-0.002	-0.004	0.09	0.002	0.002	
0.087	-0.002	-0.004	0.085	-0.002	0.002	0.082	0.002	0.002	
0.078	0.002	-0.002	0.071	-0.002	-0.002	0.065	0.002	-0.002	
Half SIGNAL LENGTH IN Θ DIRECTION $L_\Theta = 1.571$ RADIANS									
FFT IN Z-DIRECTION N=1,9									
λ_z	C	D	λ_z	C	D	λ_z	C	D	
1.00	0.002	-0.012	0.5	0.002	-0.006	0.33	-0.008	-0.008	
0.25	-0.004	-0.006	0.2	-0.016	0.008	0.17	-0.002	0.002	
0.14	-0.004	0.002	0.13	-0.002	0.002	0.11	-0.002	0.002	
HALF SIGNAL LENGTH IN Z DIRECTION $L_z = 0.5$ INCH									

TABLE (5)

$A_0 = 0.149$ All Dimensions in inches									
FFT IN X-DIRECTION M=1,29									
λ_x	A	B	λ_x	A	B	λ_x	A	B	
9.34	-0.050	-0.004	4.69	0.006	0.006	3.13	0.000	0.024	
2.34	-0.016	0.000	1.87	0.006	-0.002	1.56	-0.004	-0.022	
1.34	0.010	0.008	1.17	0.010	0.000	1.04	-0.014	-0.010	
0.94	0.002	0.000	0.85	0.002	-0.004	0.62	0.002	-0.004	
0.72	0.000	-0.002	0.67	-0.002	0.006	0.55	-0.002	0.000	
0.52	0.002	0.008	0.49	0.006	-0.004	0.47	-0.008	0.002	
0.43	0.002	0.004	0.41	0.008	0.000	0.39	-0.008	0.000	
0.35	0.002	-0.002	0.33	-0.006	0.000	0.32	0.006	0.000	
0.31	0.004	0.000	0.29	-0.006	0.002	0.28	0.006	0.002	
0.26	0.004	0.000	0.23	-0.004	0.000				
HALF SIGNAL LENGTH IN X DIRECTION $L_x = 4.686$ INCHES									
FFT IN Y-DIRECTION N=1,6									
λ_y	C	D	λ_y	C	D	λ_y	C	D	
1.0	0.004	-0.012	0.5	0.002	-0.006	0.33	-0.004	-0.006	
0.25	0.000	-0.006	0.2	-0.014	0.002	0.17	-0.002	0.000	
HALF SIGNAL LENGTH IN Y DIRECTION $L_y = 0.5$ INCHES									

TABLE (6)

Coordinates of 5 minute glaze ice on NACA 0012 Chord of airfoil C = 21.125 inches X, Y---- All dimensions in inches								
X	Y	X	Y	X	Y	X	Y	
2.94	1.1	0.653	0.629	-0.076	-0.597	2.086	-0.993	
2.722	1.079	0.464	0.56	0.123	-0.825	2.297	-1.023	
2.513	1.051	0.21	0.525	0.315	-0.995	2.506	-1.05	
2.303	1.022	-0.003	0.563	0.541	-1.12	2.717	-1.074	
2.087	0.992	-0.211	0.605	0.619	-1.112	2.94	-1.093	
1.872	0.955	-0.436	0.629	0.834	-1.057			
1.667	0.914	-0.515	0.603	1.039	-0.993			
1.458	0.87	-0.558	0.354	1.257	-0.926			
1.25	0.819	-0.466	0.082	1.46	-0.885			
1.032	0.758	-0.368	-0.146	1.665	-0.916			
0.855	0.699	-0.225	-0.386	1.881	-0.956			

Heater and thermocouple location					
#	1/C	#	1/C	#	1/C
1	-0.019	6	0.006	11	0.07
2	-0.032	7	0.019	12	0.083
3	-0.045	8	0.032	13	0.096
4	-0.058	9	0.045		
5	-0.006	10	0.058		

REFERENCES

1. _____, "Aircraft Icing," AGARD-AR-127, Ottawa, Canada, 1977.
2. _____, "Icing Testing for Aircraft Engines," AGARD-CP-236, London, United Kingdom, 1978.
3. _____, *American Institute of Aeronautics and Astronautics, Aerospace Sciences Meeting*, 19th, St. Louis, MO, January 1981.
4. Olsen, W., Shaw, R. and Newton, J., "Ice Shapes and the Resulting Drag Increase for a NACA 0012 Airfoil," NASA-TN-83556, 1984.
5. Bragg, M.B., Gregorek, G.M. and Shaw, R.J. "Windtunnel Investigation of Airfoil Performance Degradation Due to Icing," AIAA-82-0582, 1982.
6. Laschka, B. and Jesse, R.E., "Ice Accretion and its Effects on Aerodynamics of Unprotected Aircraft Components," AGARD-AR-127, section 4, 1977.
7. Hood, M.J., "The Effects of Some Common Surface Irregularities on Wing Drag," NACA-TN-695.
8. Jacobs, E.N., "Airfoil Section Characteristics as Affected by Protuberances," NACA-TR-446.
9. Ashwood, P.F., and Swift, R.D., "Icing trials on the Front Fuselage and Engine Intakes of Helicopters at Conditions Simulating Forward Flight," AGARD-AR-127, section 3, 1977.
10. Vath, K.A., "Meteorological Icing Conditions," AGARD-CP-236, section 3, April, 1978.

11. Kchlman, D.L., Schweikhard, W.G. and Albright, A.E., "Icing Tunnel Tests of a Glycol Exuding Porous Leading Edge Ice Protection System on a General Aviation Airfoil," *NASA-CR-165444*, 1981.
12. Ringer, T.R. and Stallabrass, J.R., "The Dynamic Ice Detector for Helicopters," *AGARD-CP-236*, section 8, 1978.
13. Grabe, W. and Tedstone, D., "Icing Tests on a Small Gas Turbine with Inertial Separation Anti-Icing System," *AGARD-CP-236* section 13, 1978.
14. Dewitt, K.J. and Baliga, G., "Numerical Simulation of One Dimensional Heat Transfer in Composite Bodies with Phase Change," *NASA-CR-165607*, 1982.
15. Schmitt, D.A., "Subscale Tests of an Ice Suppression System for Space Shuttle Launches from Vandenburg Airforce Base," *AIAA-84-0610*.
16. Rosenthal, H.A. and Nelepoivitz, D.O., "Performance of a New Nose-Lip Hot-Air Anti Icing Concept," *AIAA-85-1117*.
17. Kleuters, W. and Wolfer, G., "Some Recent Results on Icing Parameters," *AGARD-AR-127*, 1977.
18. Hankey, W.L. and Kirchner, R., "Ice Accretion of Wing Leading Edges," *AFFOL-TM-79-85-FXM*, June 1979.
19. Wilder, R.W., "A Theoretical and Experimental Means to Predict Ice Accretion Shapes for Evaluation of Aircraft Handling and Performance Characteristics," *AGARD-AR-127*, section 5, 1977.
20. Shaw, R.J., Sotos, R.G. and Solano, F.R., "An Experimental Study of Airfoil Icing Characteristics," *NASA-TM-82790*, 1982.
21. McDevitt, J.B. and Okuno, A.F., "Static and Dynamic Pressure Measurements on a NACA 0012 Airfoil in the Ames High Reynold's Number Facility," *NASA-TP-2485*.

22. Bragg, M.B., Gregorek, G.M. and Shaw, R.J., "An Analytical Approach to Airfoil Icing," *AIAA-81-0403*, 1981.
23. Schlichting, H., *Boundary Layer Theory*, Chap. 12, 6th Ed., 1968, McGraw Hill.
24. Messinger, B.L., "Analysis of an Unheated Icing Surface," *J. of the Aeronautical Sciences*, vol 20, pg 29, 1953.
25. Van Fossen, G.J., "Design of Experiments for Measuring Heat Transfer Coefficients with a Lumped-Parameter Calorimeter," *NASA-TN-D-7837*, 1975.
26. Incropera, F.P. and DeWitt, D.P., *Fundamentals of Heat Transfer*, John Wiley, pp. 340-350, 1981.
27. Kays, W.M. and Crawford M.E., *Convective Heat and Mass Transfer*, 2nd Edition, McGraw Hill, pp. 139-158, 1980.
28. Abdelghany, M. M., "Experimental Study of Axial Flow in a Finite Array of Rods and the Application of Finite Element Techniques to Flow in Ducts and Rod Bundles," *Ph.D. Thesis*, University of Kentucky, Lexington, KY, pp. 27-29.
29. Arimilli, R.V. and Keshok, E.G., "Measurements of Local Convective Heat Transfer Coefficients on Ice Accretion Shapes," *AIAA-84-0018*, 1984.
30. Shaw, J., NASA, Lewis Research Center, Cleveland, OH 44135.
31. Van Fossen, G.J., Simoneau, R.J., Olsen Jr., W.A. and Shaw, R.J., "Heat Transfer Distributions around Nominal Ice Accretion Shapes Formed on a Cylinder in the NASA Lewis Icing Research Tunnel," *NASA-TM-83557*, 1984.
32. Calarese, W. and Barth, J.T., "Numerical Simulation of Heat Transfer Rates on an Ice Accretion Model," *AFWAL-TM-85-191-FIMM*, 1985.
33. Marks' Standard Handbook for Mechanical Engineers, Chapter 13, 8th ed.

34. Rosenfeld, A., "Automatic Recognition of Basic Terrain Types from Aerial Photographs," *Photogrammic Engineering*, 28, 1, March 1962.
35. Lendaris, G.G., and Stanley, G.L., "Diffraction Pattern Sampling for Automatic Pattern Recognition," *Proc. IEEE*, 58, 2, pg198-216, Feb 1970.
36. Oppenheim, A.V. and Schafer, R.W., *Digital Signal Processing*, Prentice Hall, 1975.
37. Lighthill, M.J., *Fourier Analysis and Generalised Functions*, Cambridge Univ. Press.
38. Pratt, W.K., *Digital Image Processing*, John Wiley, 1978.
39. Andrews, H.C., *Computer Techniques in Image Processing*, 1970, Academic Press.
40. Ahmed, N. and Rao, K.R., *Orthogonal Transforms for DSP*.
41. Cooley, J.W., Lewis, P.A.W., and Welch, P.D., "Historical notes on the Fast Fourier Transform," *Proc. of the IEEE*, Vol. 55, No. 10, October 1967.
42. Perry, A.E., Schofield, W.H. and Joubert, P.N., "Rough Wall Turbulent Boundary Layers," *J. of Fluid Mechanics*, Vol. 37, 1969.
43. Schlichting, H., "Experimental Investigation of the Problem of Surface Roughness," *NACA-TM-823*, 1936.
44. Nikuradse, J., "Laws of Flow in Rough Pipes," *NACA-TM-1292*, 1933.
45. Coleman, H.W., Hodge, B.K., and Taylor, R.P., "A ReEvaluation of Schlichting's Surface Roughness Experiment," *Trans. of the ASME*, Vol. 106, March 1984.
46. Rotta, J.C., "Turbulent Boundary Layers in Incompressible Flows," *Progress in Aeronautical Sciences*, Vol. 2., 221 pg, 1962.
47. Koh, J.C.Y., and Hartnett, J.P., "Measured Pressure Distribution and Local Heat Transfer Rates for Flow Over Concave Hemispheres," *ARS Journal*, pg 71, January 1961.

48. Clauser, F.H., "Turbulent Boundary Layer," *Advances in Applied Mechanics*, Vol. 4, 1956, Acad. Press.
49. Young, A.D., "The Drag Effects of Roughness at High Sub-Critical Speeds," *J.Roy.Aero.Soc.*, page 534, 1950.
50. Pimenta, M.M, Moffat, R.J., and Kays, W.M., "The Structure of a Boundary Layer on a Rough Wall with Blowing and Heat Transfer," *J.of Heat Transfer*, vol. 101, pg 193, May 1979.
51. Nikitin, I.K., "Heat and Mass Transfer in the Turbulent Boundary Layer of a Surface with Arbitrary Roughness Properties," *Heat Transfer Soviet Research*, vol. 5, No. 3, May-June 1973.
52. Domanov, V.N., "The Temperature Distribution in the Thermal Boundary Layer Above Surfaces with Wavy Roughness," *Heat Transfer Soviet Research*, Vol. 8, No. 6, Nov-Dec, 1976.
53. Deacon, E.L. and Webb, E.K., "Interchange of Properties between Sea and Air," *The Sea*, Ch. 3, Vol. 1, Ed. M.N. Hill, Interscience Publ., 1962.
54. Bragg, M., "Experimental Flowfield Measurements," *Airfoil Performance In Icing Workshop*, NASA, Lewis, 1985.



6 - 8 7

110

